12-10-2022

IMPROVING NEAR SURFACE REFRACTIVITY ESTIMATES IN MARINE ENVIRONMENTS

Sarah Evelyn Wessinger
Coastal Carolina University

IMPROVING NEAR SURFACE REFRACTIVITY ESTIMATES IN MARINE ENVIRONMENTS

By

Sarah Evelyn Wessinger

Submitted in Partial Fulfillment of the

Requirements for the Degree of Master of Science in

Coastal Marine and Wetland Studies in the

School of the Coastal Environment

Coastal Carolina University

2022

_____	_____
Erin Hackett, Ph.D.	Craig Gilman, Ph.D.
Major Advisor	Committee Member
_____	_____
Roi Gurka, Ph.D.	Chad Leverette, Ph.D.
Committee Member	Dean, Gupta College of Science

_____
Erin Hackett, Ph.D.
CMWS Graduate Program Director

Dedication

For my family who supports and cheers me on endlessly.

For my friends who became family.

For my dog, Gunny, who kept me sane.

Acknowledgments

I would like to endlessly thank my advisor Dr. Erin Hackett for her priceless guidance and dedication into molding me into a competent and confident scientist. Without her relentless support and advice, I would not be the woman in STEM I am today. I would also like to thank my committee members, Dr. Roi Gurka and Dr. Craig Gilman, for their unique perspectives. I would also like to thank Tracy Haack from the Naval Research Lab for providing COAMPS®-NAVSLaM data for this study, Dr. Qing Wang from the Naval Postgraduate School for providing *in-situ* CASPER-East data, and Dr. Robert Burkholder from The Ohio State University for providing the *in-situ* radar data.

I would also like to acknowledge all my colleagues in the Environmental Fluids Laboratory for their collaboration, counsel, and comradery. I also want to specifically thank members of the radar team, Daniel Greenway, Douglas Pastore, and Mathew Stanek for providing me with numerous opportunities to publish, do fieldwork, and grow as a team-oriented scientist as well as their endless support in offering advice, edits, and discussion. I would also like to thank various other graduate students and scientists for their unique perspectives and the privilege of working and studying with them: Mary Olsen, Zachary Czoer, Meredith Pfennig, and Zeke Meyers.

I would also like to thank the Office of Naval Research for providing partial funding for this study (grants: N00014-16-1-2075, N00014-19-1-2350) as well as Coastal Carolina University for other various funding contributions and support.

Abstract

This study utilizes *in-situ* measurements and numerical weather prediction datasets collected during the *Coupled Air-Sea Processes Electromagnetic Ducting Research* East field campaign to assess how thermodynamic properties in the marine atmospheric surface layer influence evaporation duct shape and to develop a simple near-surface modified refractivity estimation method. This study utilizes a logarithmic linear parametric model, which describes evaporation ducts via three main parameters: evaporation duct height, evaporation duct curvature, and mixed layer slope. Notably, most studies utilizing this type of model assume the curvature, C_0, to be a theoretical value derived assuming neutral atmospheric stability; a thermodynamic regime that is rarely observed precisely. Prior studies suggest varying C_0 to represent a wider range of ED shapes. Unfortunately, the physical significance of C_0 is poorly understood so this approach is not commonly adopted. This study investigates relationships between C_0 and near surface thermodynamic properties. The relationship between C_0 and the air-sea temperature difference (ASTD) reveal, during unstable periods, that C_0 are generally greater than in near-neutral or stable environments. C_0 in near-neutral environments are generally close to the theoretical value. The linear relationship between the near surface specific humidity gradient (NSSHG) and C_0 is stronger than that with ASTD thus, it is concluded that C_0 variations are primarily driven by NSSHG. Modified refractivity profiles are modeled using C_0 based on a NSSHG empirical linear model (termed, EDS model) and compared to other common methods of near surface estimation such as Monin-Obukhov similarity theory (MOST) and extrapolation from ~3m to the surface. Refractivity estimated from the EDS model was similar to *in-situ* refractivity measurements. Linearly or non-linearly (i.e., polynomials)

extrapolating refractivity to the surface resulted in closer agreement between measured and modeled propagation loss, indicating that measured data better predicted PL than either model. Notably, the EDS model predicted PL that is statistically similar to that predicted by MOST implying this novel empirical method is a practical alternative to MOST in applications such as propagation modeling and requires significantly less environmental measurements.

Table of Contents

List of Figures

List of Symbols and Abbreviations

Atlantic Explorer:	*AE*
Average Second Order Derivative of COAMPS® Modified Refractivity Profiles with Altitude:	ASOD
Air-Sea Temperature Difference:	ASTD
Evaporation Duct Curvature:	C_0
Y-intercept of Linear Fit Between C_0 and NSSHG:	C_{0y}
Coupled Air-Sea Processes and Electromagnetic Ducting Research:	CASPER
Number of Compared MAPS Modified Refractivity Profiles in the Two-Sample T-Test:	C_{Mref}
Coupled Ocean Atmosphere Mesoscale Prediction System®:	COAMPS®
Coupled Ocean Atmosphere Response Experiment:	COARE
Degrees of Freedom:	d_f
Electric Field in the Environment:	$\boldsymbol{E}$
Partial Vapor Pressure:	e
Saturation Vapor Pressure	e_s
Electric Field in Free Space:	$\boldsymbol{E_0}$
Mean Squared Error:	E_r
Evaporation Duct:	ED
Evaporation Duct Height:	EDH
Evaporation Duct Shape:	EDS
Electromagnetic:	EM
Correction Factor to Account for Difference in Pressure due to a Mixture of Vapor and Air Over Water:	f

One-way Pattern Propagation Factor:	F
Receiver Peak Power Gain:	G_r
Transmitter Peak Power Gain:	G_t
Significant Wave Height:	h_s
von Karman Constant:	k
Electromagnetic Wavenumber:	k_0
Monin-Obukhov Length:	L
Modified Refractivity:	M
Integral of Mean Wave Spectrum:	m
Modified Refractivity Estimated from the Parametric Model:	$\widehat{M}$
Continuity Term:	M_1
Mixed Layer Slope:	m_1
Marine Atmospheric Profiling System:	MAPS
Marine Atmospheric Surface Layer:	MASL
Modified Refractivity Profiles of COARE or COAMPS®:	M_c
M-Deficit for an Elevated Duct:	M_d
Surface Value of Modified Refractivity:	M_0
Monin-Obukhov Similarity Theory:	MOST
Mean Squared Error:	MSE
Atmospheric Refractivity:	N
Index of Refraction:	n
Navy Atmospheric Vertical Surface Layer Model:	NAVSLaM

Number of Points in a Modified Refractivity Profile Up to the Duct Height:	n_{mref}
Number of Propagation Measurements:	n_{prop}
Near Surface Specific Humidity Gradient:	NSSHG
Near Surface Specific Humidity Gradient Calculated for COAMPS® based on points at $z = 0.1Z_d$ and $z = 2Z_d$:	$NSSHG_{0.1}$
Near Surface Specific Humidity Gradient Calculated for COAMPS® based on points at $z = 0.25Z_d$ and $z = 2Z_d$:	$NSSHG_{0.25}$
Pressure:	p
Propagation Loss:	PL
Propagation Loss:	P_L
Received Power:	P_r
Transmitted Power:	P_t
Average Specific Humidity:	$\bar{q}$
Specific Humidity Scaling Factor:	q_*
Surface Specific Humidity:	q_s
Slant Range:	R
Coefficient of Determination:	R^2
Research Vessel:	R/V
Radius of the Earth:	R_e
Radio Frequency:	RF
Relative Humidity:	R_H
Measured Propagation Loss:	R^m
Simulated Propagation Loss:	R^s

Root Mean Squared Error:	RMSE
Receiver Height:	Rx
Standard Deviations of Simulated EDS PL RMSEs:	S_{M1}
Standard Deviations of Simulated MAPS, MOST, and Linear Extrapolation Methods PL RMSEs:	S_{M2}
Sea Surface Temperature:	SST
Skin Sea Surface Temperature:	T_s
Temperature:	T
T-Statistic:	t
Temperature Scaling Factor:	T_*
Average Temperature:	$\overline{T}$
Wind Speed:	U
Wind Scaling Factor:	U_*
Ocean Surface Current:	U_s
Average Wind Velocity:	$\overline{U}$
Variable Terrain Radio Parabolic Equation:	VTRPE
Altitude above Mean Sea Level:	z
Evaporation Duct Height:	Z_d
Aerodynamic Roughness Factor:	z_0
Specific Humidity Roughness Length:	z_{0q}
Temperature Roughness Length:	z_{0T}
Thickness of Inversion Layer for an Elevated Duct:	z_{thick}
Bottom of the Inversion Layer in an Elevated Duct:	z_1

Top of the Inversion Layer in an Elevated Duct:	z_2
Evaporation Layer Height:	z_L
Slope of Linear Fit between NSSHG and C_0:	α
Vertical Gradient of Modified Refractivity:	$\frac{\partial M}{\partial z}$
Average Second Order Derivative of COAMPS® Modified Refractivity Profiles with Altitude:	$\overline{\frac{\partial^2 M}{\partial z^2}}$
Universal Stability Function of Specific Humidity:	Φ_q
Universal Stability Function of Temperature:	Φ_T
Universal Stability Function of Wind Speed:	Φ_U
Integrated Form of the Universal Stability Function of Specific Humidity:	Ψ_q
Near Surface Specific Humidity Gradient:	Ψ_s
Integrated Form of the Universal Stability Function of Temperature:	Ψ_T
Integrated Form of the Universal Stability Function of Wind Speed:	Ψ_U
Root Mean Squared Error:	Ω
Mean Simulated PL RMSE for EDS Method:	$\overline{\Omega_{M1}}$
Mean PL RMSE for Simulated MAPS, MOST, or Linear Extrapolation Methods:	$\overline{\Omega_{M2}}$

1.0 Introduction

Electromagnetic (EM) waves are used in everyday applications such as weather forecasting, cell phone communications, military defense, and commercial air travel. In the marine atmospheric surface layer (MASL), i.e., within ~100 m of the sea surface, effects of a constantly varying medium on EM waves are intricate due to the air's turbulent nature and complex air-sea interactions.

EM waves are influenced by thermodynamic fluctuations in air properties, specifically, temperature, pressure, and humidity. These properties vary the range and strength of received EM signals by varying the index of refraction, which changes the direction of EM signal propagation resulting in anomalies within the expected EM signal patterns compared to a standard atmosphere. Modified refractivity is commonly used to describe the index of refraction within the MASL (Skolnik, 2003) and is defined as the deviation of the index of refraction from that in a vacuum relative to Earth's curvature (Karimian et al., 2013). When modified refractivity decreases with altitude, a ducting scenario is present which causes signal refraction towards the Earth's surface (Skolnik, 2003; Karimian et al., 2013) resulting in target positioning errors, signal loss above the duct, and expanded signal range within the duct. Evaporation ducts (EDs) are the most common type of duct in the MASL (Skolnik, 2003), which are surface ducts driven by rapid decreases of humidity with altitude. EDs strongly influence the performance of X-band sensors and communication systems; therefore, accurately describing EDs is critical.

Measuring near surface thermodynamic properties for this complex environment is uniquely difficult; current technologies often have too-coarse spatiotemporal resolution to accurately capture rapid changes in air properties as the sea surface is approached. These limitations primarily result from platform interference, sensor housing size, and sensor damage due to harsh conditions. To compensate for this limitation, methods such as linear extrapolation, polynomial fits, and Monin-Obukhov similarity theory (MOST) are employed to extend measurements a few meters above the surface to the surface; yet these methods also have shortcomings such as not being grounded in the physics of the MASL or, in the case of MOST, requiring many bulk measurements which is not always practical. MOST is a boundary layer similarity solution for wind, temperature and humidity with empirically derived constants and employs the Monin-Obukhov length, an important length scale (Monin and Obukhov, 1954; Foken, 2006). Its implementation requires several bulk environmental measurements.

For propagation modeling purposes, another common approach for estimating modified refractivity is using log-linear ED models, which describe EDs with a limited number of parameters. A two-layer refractivity model proposed by Penton and Hackett (2018; Eqn. 7) defines EDs using three parameters: duct height (Z_d), duct curvature (C_0), and mixed layer slope (m_1). Currently, there is no way to estimate the curvature of a modified refractivity profile (C_0) *a priori* via atmospheric measurements due to its unknown connection to the physical environment. In most current research on EM wave propagation, the value for the duct curvature (C_0) is assumed to be 0.125 M-units m^{-1}, which is defined as the critical gradient for trapping (Paulus, 1990) and was derived under the assumption of a rarely observed thermodynamically neutral atmosphere (Paulus, 1990). Variations in

C_0 impact EM wave propagation as shown in the global sensitivity study by Lentini and Hackett (2015) and the study by Pastore et al. (2021); therefore, the ability to reasonably estimate C_0 will improve the accuracy of using simple log-linear models to describe EDs.

All the aforementioned methods (i.e., MOST, linear fits, polynomial fits, and log-linear models) all have their unique strengths and weaknesses as they each employ different assumptions and have various limitations; thus, the model most appropriate will depend on the application. Parametric models are often used in propagation modeling due to their simplicity and easy integration into propagation simulations but are limited in how the refractivity profile can be modified (i.e., constrained by the parameters in the model). This study focuses on improving this parametric model approach by allowing more flexibility in the parametric model via adjustment of duct shape for a given duct height.

More specifically, this research examines the physical significance of duct curvature and links this parameter to bulk environmental measurements by evaluating numerical datasets for relationships between near surface thermodynamic gradients and C_0. Finding quantifiable relationships between environmental measurements and duct curvature enables development of a model to estimate duct curvatures that are reasonably representative of *in-situ* measurements and thus different atmospheric stabilities.

The developed C_0 model characterizes the MASL directly above the surface based on the near surface specific humidity gradient (NSSHG) due to the strong direct relationship between C_0 and NSSHG and is simpler than current methods (i.e., MOST) due to requiring less *in-situ* measurements. In unstable conditions, the developed method also predicts a larger C_0 than the neutral value derived by Paulus (1990). Simulated propagation loss (PL) using modified refractivity based on this developed C_0 model is compared to simulated PL

of other current methods of extending coarse resolution data to the surface. The developed model preformed statistically similar to MOST.

This thesis is organized in the following manner: the next section provides background information, the third section outlines the research objectives, followed by the methods section which discusses data sources and analysis methods, results are presented next, then it concludes with a summary.

2.0 Background

The following subsections provide background information on topics relevant to this research including radar wave propagation (§2.1), environmental effects on radar wave propagation (§2.2), a review of modified refractivity modeling (§2.3), and a review of current literature on near surface refractivity estimation methods (§2.4).

2.1 Electromagnetic Wave Propagation

Radar is transmitted in two configurations, monostatic and bistatic. For monostatic radar, the transmitter and receiver are in the same location, whereas for the focus of this study, bistatic radar, the receiver is in a separate location than the transmitter. X-band radar propagation in bistatic radar systems is described by the one-way radar transmission equation (Friis, 1946; Freehafer et al., 1951):

$$\frac{P_r}{P_t} = G_t G_r \left[\frac{F}{2\ k_0 R}\right]^2 \tag{1}$$

where P_r/P_t is the ratio of received power (P_r) to transmitted power (P_t), F is the one-way pattern propagation factor, G_t is the transmitter peak power gain, G_r is the receiver peak power gain, k_0 is the EM wavenumber, and R is the slant range from the receiver to the transmitter. G_t, G_r, P_r, P_t, R, and k_0 are determined by the setup of the specific radar system, whereas F is a consequence of the environment. Notably, F is a large term influencing the power ratio, implying the key role the environment plays in received power. One-way propagation factor (F) is defined as the magnitude of the ratio of the electric field in the environment ($\boldsymbol{E}$) to the electric field in free space ($\boldsymbol{E_0}$):

$$F = \left|\frac{\boldsymbol{E}}{\boldsymbol{E_0}}\right| \tag{2}$$

Propagation loss (P_L) is the logarithmic difference (i.e., a ratio in a non-logarithmic space) between the propagation factor in the environment and the propagation factor in a vacuum (Skolnik, 1990):

$$P_L = 20\log(2k_0R) - 20\log|F| \tag{3}$$

Thus, P_L is a measure of the effects of the environment on the received radar power. Understanding how radar signal propagation is affected by the environment is imperative to the optimization of radar systems.

2.2 Environmental Effects on Radar Wave Propagation

Major environmental effects on radar propagation are reflection, scattering, absorption, and refraction. Interaction with a surface causes reflection, resulting in a phenomenon known as multipath, and EM wave scattering (Skolnik, 2003). Multipath occurs when the signal has two potential paths it can travel to the same location; the direct path, which is the straight-line path from the radar antenna to the receiver and the indirect path, where the radar wave reflects off a surface and reaches the receiver. Constructive interference occurs when two signals reach the receiver in-phase whereas destructive interference occurs when the waves reach the receiver perfectly out-of-phase resulting in total signal loss. This constructive and destructive pattern depends on the wavelength of the radar wave and the relative distance between the two paths, i.e., on the range and height of the target or receiver. Thus, a PL pattern shows what is referred to as a "lobing" pattern due to these locations of constructive and destructive interference as seen in Figure 1. The "lobes" refer to constructive interference and therefore, the least amount of PL. Between the "lobes" there are regions of destructive interference known as "nulls" that have the largest PL.

Absorption occurs when the energy of an EM wave is absorbed by the environment and most commonly occurs via gas molecules such as water vapor. For example, when the EM wave wavelength is close to water vapor molecule size, the molecules absorb energy from the EM wave. In this process, energy is transferred from the EM wave to the molecule causing a decrease in the received EM wave signal strength and thus an increase in PL. In the absence of precipitation, absorption is negligible at X-band frequency (i.e., 8 GHz to 12 GHz) due to EM wavelength being on the order of centimeters.

Most importantly, X-band EM waves are affected by refraction which is a change in the EM wave's propagation direction due to a varying medium. This change in direction can have beneficial and detrimental implications during extreme refraction scenarios, known as ducts, which trap EM waves near the Earth's surface and cause extended signal range and target positioning errors. The extent of the EM waves direction change is dependent on the gradient of the index of refraction, which fluctuates with the thermodynamic properties of the atmosphere.

Thermodynamic properties in the MASL are constantly changing due to phenomena such as fronts, high/low pressure systems, and sea/land breezes. Atmospheric refractivity (N) is related to the atmospheric thermodynamic properties of pressure, temperature, and humidity through (Bean and Dutton, 1968):

$$N = 77.6\frac{p}{T} + 373{,}256\frac{e}{T^2} \tag{4}$$

where p is pressure (mb), T is temperature (K), and e is partial vapor pressure (mb). In the MASL, humidity and temperature generally have the largest influence on refractivity variations since p varies little in comparison.

Atmospheric stability, which is relevant to the expected refraction regime, is influenced by

various thermodynamic factors such as changes in air temperature and humidity. Stability is the tendency of a fluid to return to its original state once perturbed and is determined by the fluid's density gradients; when a fluid is stable and perturbed, it tends to return to its original state, whereas when a fluid is unstable and perturbed it does not return to its original state. This study utilizes the air-sea temperature difference (ASTD) as a stability metric and thus assumes the dominating factor on atmospheric stability is temperature. In the atmosphere there are three possible thermal stability regimes: stable, unstable, and neutral. A stable regime occurs when the air is warmer than the ocean surface; this suppresses vertical motion by requiring additional energy to overcome density gradients and leads to low turbulence intensities. An unstable regime takes place when the atmosphere is cooler than the ocean surface; facilitating vertical motion, mixing, and turbulence, and when temperatures differences are large enough, leads to development of convection cells. A neutral regime occurs when the atmosphere is the same temperature as the ocean surface; this condition is rarely observed precisely, although near-neutral conditions can be common.

Refractive environments are classified into several regimes: standard refraction, sub-refraction, super-refraction, and trapping/ducting conditions, each defined by the gradient of atmospheric refractivity with altitude. Sub-refraction and ducting conditions are normally observed during unstable atmospheric conditions and super refraction is normally observed during stable atmospheric conditions (Paulus, 1991; Trahan, 1995).

Standard refraction causes radar waves to slightly bend away from Earth's surface. Sub-refraction occurs when the refraction gradient is positive, and this causes the radar waves to promptly diverge from the Earth's surface. Super-refraction causes radar waves to bend

towards Earth's surface slightly more than under standard conditions, but ultimately still diverge due to Earth's curvature. When trapping or ducting conditions occur, radar waves bend towards the Earth's surface, bouncing off Earth's surface so that radar wave energy is trapped near the surface as exemplified in Figure 2. Large negative refractivity gradients occur in trapping conditions; trapping a radar wave's energy can significantly extend the range of a radar system (Skolnik, 2003; Kukushkin, 2004).

When trapping is bound by the Earth's surface, it is known as a surface duct whereas elevated ducts occur when a trapping layer is not directly at the surface, as shown in Figure 3; elevated ducts are often found between 30° north and 30° south latitudes (Skolnik, 2001). The most common type of surface duct in marine environments is an ED, which occur due to a rapid decrease in humidity with altitude (Skolnik, 1990; Skolnik, 2003). ED's are known to cause extended signal range within the duct, signal loss above the duct, and positioning errors. Positioning errors can be caused, for example, by the radar system not accounting for the expanded range of the radar system due to signal trapping.

To easily identify ducts, modified refractivity (M) is commonly used because it accounts for the curvature of the Earth:

$$M(z) = \left(n + \frac{z}{R_e} - 1\right) \times 10^6 = N + \frac{z}{R_e} \times 10^6 \tag{5}$$

where n is the index of refraction, z is altitude, and R_e is the radius of the Earth.

EDs are easily observed when presented in units of modified refractivity because a duct is present anytime the gradient of modified refractivity with height is negative. Evaporation duct height (EDH) is defined as the altitude in which the vertical gradient of modified refractivity is zero as exemplified in Figure 4a. Resulting radar wave propagation for a 10.3 m X-band transmitter for an ED with an EDH of 10.1m is shown in Figure 4b, where

reduced PL below the EDH out to 60 km is evident.

2.3 Modeling the Refractive Environment

There are multiple ways to forward model the refractive environment including numerical weather prediction models and bulk environmental models. Bulk environmental models require some basic meteorological measurements whereas numerical weather prediction models may also use meteorological measurements for data assimilation. Primary limitations of numerical weather prediction models include coarse spatiotemporal resolutions, and approximations for small-scale processes; while limitations of bulk environmental models include the need for direct measurements, and limits to their applicability outside the range of conditions in which empirical relationships were developed.

Parametric refractivity models are commonly used in propagation modeling (Sirkova, 2012). Gerstoft et al. (2003) used a model that accounts for both evaporation and elevated ducting conditions:

$$M(z) = M_0 + \begin{cases} M_1 + C_0\left(z - Z_d ln\left(\frac{z+z_0}{z_0}\right)\right), & z < z_L \\ m_1 z, & z_L \le z < z_1 \\ m_1 z_1 - M_d\left(\frac{z+z_1}{z_{thick}}\right), & z_L \le z < z_2 \\ m_1 z_1 - M_d + m_3(z - z_2), & z_2 \le z \end{cases} \quad (6)$$

where z_L is the evaporation layer height equal to twice the duct height, z_1 is the bottom of the inversion layer in an elevated duct (Figure 3B), z_2 is the top of the inversion layer in an elevated duct, z_0 is the aerodynamic roughness factor, which is commonly assumed to be 0.0015 m, $z_{thick} = z_2 - z_1$, M_d defines the M-deficit in the elevated duct, M_0 is surface modified refractivity, M_1 ensures continuity in the profile between layers, and Gerstoft et al. (2003)

set C_0, the curvature parameter, to a constant value of 0.125 M-units m^{-1} as derived by Paulus (1990). The ED *M*-deficit is defined as the difference between *M* at the surface and *M* at the EDH. The mixed layer is located above the trapping layer and is defined by Gerstoft et al. (2003) as the layer where humidity and potential temperature largely do not vary with height. For elevated ducts, the mixed layer is directly below the inversion layer where the elevated duct exists.

There are numerous ED models that are a variant of Eqn. 6 (Saeger et al., 2015). One such example is a two-layer model proposed by Penton and Hackett (2018) and Matsko and Hackett (2019):

$$M(z) = M_0 + \begin{cases} C_0\left(z - Z_d ln\left(\frac{z+z_0}{z_0}\right)\right), & z_L \leq z \\ m_1 z - M_1, & z > z_L \end{cases} \quad (7)$$

This model, unlike Eqn. 6, C_0 is not set to the fixed neutral value of 0.125 M-units m^{-1} (Paulus, 1990); the assumption of neutral atmospheric stability is unrealistic as this condition is rarely observed in practice (§ 2.2). Varying C_0 allows variation in the *M*-deficit without altering the EDH, thereby altering the shape of the *M*-profile (Penton and Hackett, 2018).

2.4 Current Limitations of Near Surface Refractivity Measurements

Recent research has shown that C_0 is important in accurately modeling *M* profiles (Saeger et al., 2015) because it significantly impacts ED shape (EDS), which impacts the refractivity gradient that in-turn impacts EM propagation (Pastore et al., 2021). In a study by Saeger et al. (2015), the accuracy of three log-linear ED models were examined and it was concluded Eqn. 6 was the most accurate due to its decoupling of C_0 and m_1; this decoupling allows more flexibility in the curvature of the duct making a more accurate PL

prediction within the duct. The importance of EDS is also confirmed in a study by Pastore et al. (2021) where the EDS was related to changes in PL; Pastore et al. (2021) also noted a direct linear relationship between duct curvature and the M-deficit, which describes the strength of the duct (Zhang et al., 2011). Despite the importance of duct curvature, and the curvature effects the parameter C_0 can have on the refractivity profile, the physical factors influencing the magnitude of the C_0 parameter are currently unknown and thus, there is no way to predict C_0 based-on *in-situ* data.

Fortunately, the physical conditions that cause and influence EDs have been heavily studied with a focus on EDH. In a study by Karimian et al. (2013), it was determined that EDH is more sensitive to the ASTD and relative humidity in warmer sea surface conditions than cold sea surface conditions. Pastore et al. (2021) found EDS and *M*-deficit show more variation between three methods of estimating refractivity in unstable conditions, whereas the three compared methods of estimating refractivity tend to be in greater agreement in near neutral conditions. Collectively due to these findings, it is expected C_0 will be related to ASTD and/or humidity.

In a report by Thews (1990), resolution limitations are also discussed for a Naval onboard integrated refractive effects prediction system which produces a hypothetical probability of detection domain that is simulated from meteorological *in-situ* data. Vertical resolution of 4 m was deemed acceptable for altitudes above 50 m, but too coarse to encompass the complexity of the environment below 50 m; it is desired for the vertical resolution below 50 m to be no more than 3 m. Better resolution or an improved ability to model low altitude evaporation ducts would increase the accuracy of this system and others like it for low altitude radar performance. Unfortunately, current measurement technologies and sensors

often have a resolution that is too coarse, or suffer from sensor or platform measurement contamination, and therefore cannot accurately capture rapid changes as the surface is approached resulting in near surface data gaps (Thews, 1990; Kang and Wang, 2016; Pastore et al., 2021).

To address data gaps near the surface, various models, and methods to estimate near surface refractive gradients of EDs have been utilized such as fitting polynomials to the data (Wang et al., 2018; Pastore et al., 2021), using Monin-Obukhov (MO) similarity theory (Saeger et al., 2015; Kang and Wang, 2016), and linearly extrapolating to the surface (Saeger et al., 2015; Pastore et al., 2021).

High resolution meteorological data, described in Wang et al. (2018) and Pastore et al. (2021), measured refractivity using a winched sonde from a small boat and showed individual profiles of refractivity to be highly scattered, presumably due to a combination of turbulence and measurement uncertainty. A polynomial fit to a point cloud of measurements questionably captures near surface thermodynamic gradients due to the lack of rapid humidity increase as the surface is approached (Pastore et al., 2021).

Kang and Wang (2016) note the critical importance of near surface gradients and derived a novel method based off MOST to calculate surface fluxes and average environmental profiles using a least-squares optimization method and a weighted cost function. Saeger et al. (2015) also used MOST by merging it with linearly interpolated sonde data.

This study develops and investigates an alternate method for extending data to the surface and compares it with other commonly used methods. Due to the importance and influence of C_0 on estimating propagation (Saeger et al., 2015; Pastore et al., 2021), an accurate way to estimate C_0 based on a few basic measurements and a simple model could enable a basic

parametric refractivity model to provide accurate representation of refractivity to the surface; thus, providing accurate predictions of radar PL with a simpler model.

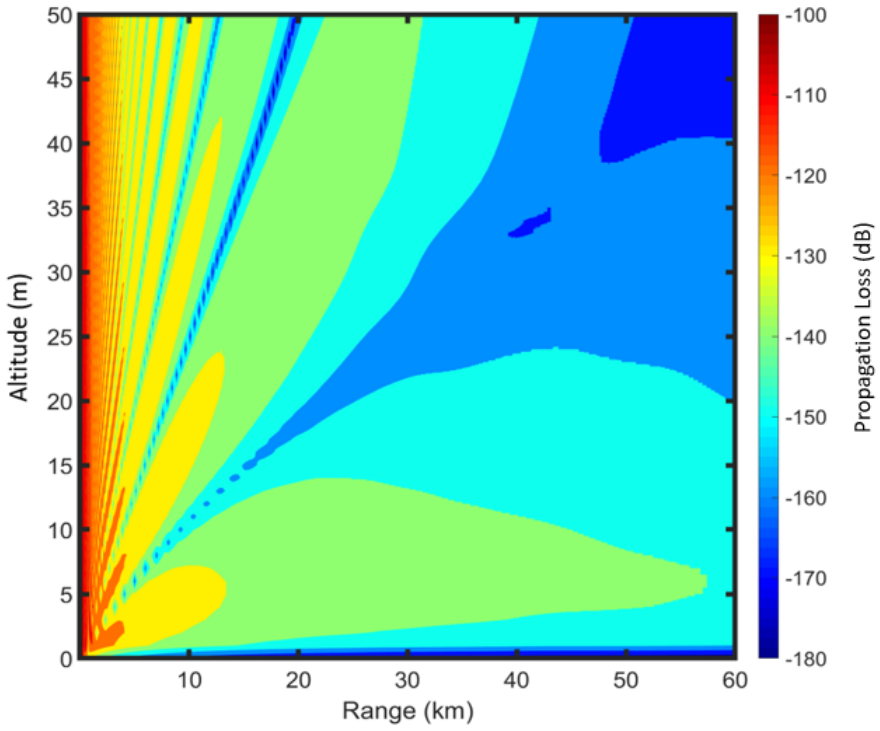

Figure 1. Propagation loss versus range and altitude. Within the domain there are noticeable "lobes" that result from multipath effects, or constructive and destructive interference.

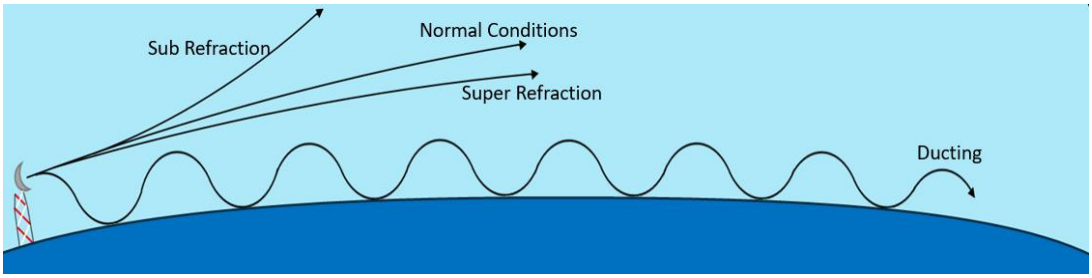

Figure 2. Refraction regimes. (Courtesy of Ian Matsko)

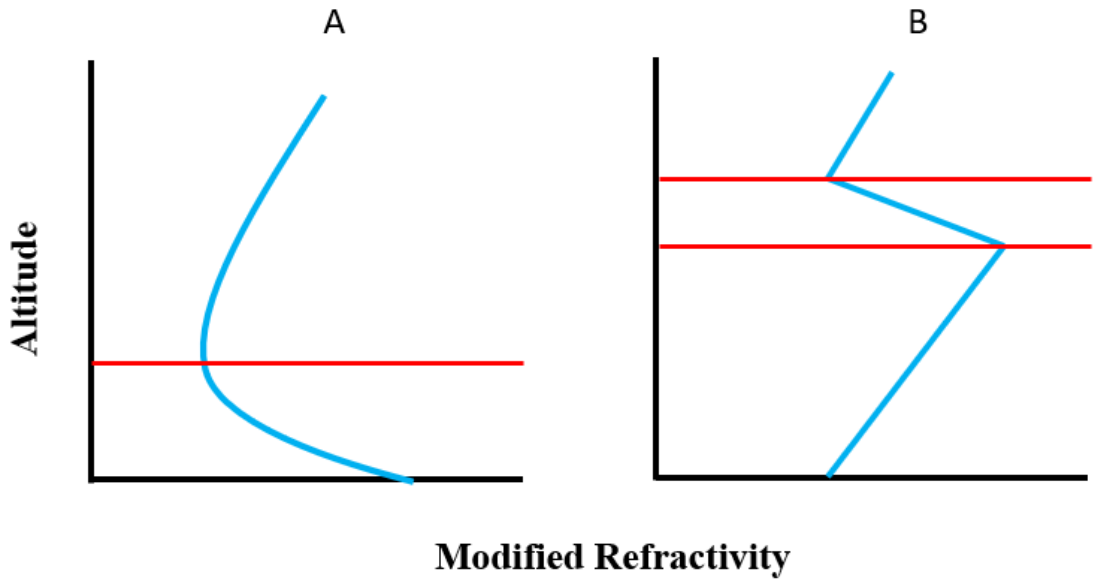

Figure 3. (A) An example of a modified refractivity profile with an evaporation duct with the top of the trapping layer denoted with red line and (B) an example of a modified refractivity profile with an elevated duct with the bounds of the trapping layer (i.e., the inversion layer) denoted with red lines.

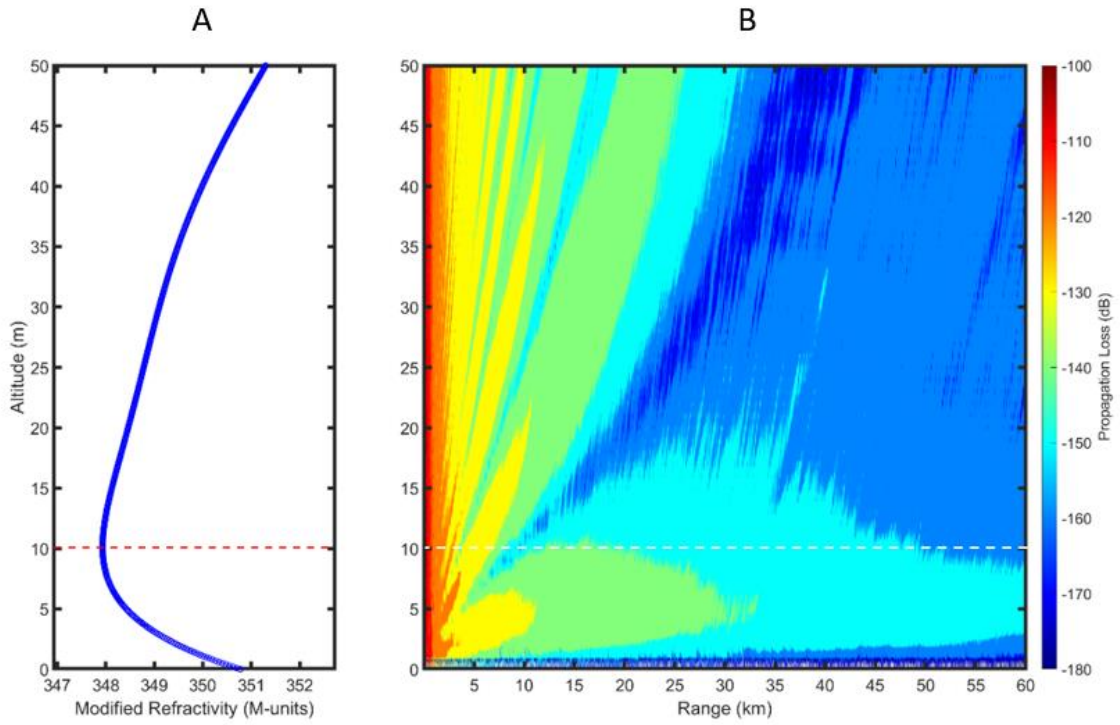

Figure 4. (A) Modified refractivity versus height with an evaporation duct height of 10.1m (red dashed line) and (B) its corresponding propagation loss pattern (duct height altitude is at the white dashed line) for a 10.3m X-band transmitter.

3.0 Research Questions

Near surface thermodynamic gradients are difficult to measure due to the air-sea interface's unsteady nature and complex interactions via waves, wind, sea spray, etc.; therefore, accurately measuring and estimating the lowest altitudes of *M* profiles is difficult. *In-situ* measurement platforms such as aerial vehicles (Fairall et al., 1996; Haack et al., 2010), tethered profiling systems (Kang and Wang, 2016; Wang et al., 2018; Babin and Dockery, 2002) and research vessels (Wang et al., 2018; Ortiz-Suslow et al., 2019) are usually unable to obtain accurate measurements within a few meters above the sea surface due to the unsteady sea surface and interference from the measurement platform leading to data gaps near the surface. Some techniques used to fill in these gaps are extrapolation and semi-empirical predictive models (Wang et al., 2018; Fairall et al., 1996; Fairall et al., 2003; Hodur, 1997).

Accurate extension of measured data to the surface is imperative because it greatly impacts the *M*-deficit and EDS, which in-turn influences propagation (Saeger et al., 2015; Lentini and Hackett, 2015; Pastore et al., 2021). To improve prediction and estimation of near surface refractivity gradients, this research targets the following hypotheses:

i. ED shape (C_0) is related to NSSHG and ASTD.

To evaluate this hypothesis, EDS is quantified by the C_0 parameter after demonstrating the relationship between C_0 and *M* profile curvature. A nonlinear least square regression is used to parameterize numerical modified refractivity profiles to the two-layer parametric

refractivity model (Eqn. 7; Penton and Hackett, 2018; Matsko and Hackett, 2019) to fit the curvature parameter (C_0) and the mixed layered slope (m_1). The fitted C_0 are used to evaluate relationships with NSSHG and ASTD. Temperature and humidity above the marine surface are mixed via mechanical processes, such as wind, to create a more uniform layer for EM wave propagation; thus, wind shear also plays a role in influencing EDs. McKeon (2013) found relative humidity and temperature are weakly related to EDH during higher wind speeds and EDH has a direct relationship with wind speed in unstable conditions, i.e., EDH increases when wind shear increases. Examining wind shear directly above the marine surface provides a more holistic picture of what processes could be dominating C_0 and the refractive environment in various thermodynamic regimes. Thus, the relationship between C_0 and wind shear are also examined.

Numerical data used for this study are generated using the Coupled Ocean Atmosphere Response Experiment (COARE, v3.0; Fairall et al., 1996; Fairall et al., 2003) algorithm, which estimates vertical profiles of temperature, wind speed, humidity, and pressure using measurements from the Coupled Air-Sea Processes and Electromagnetic Ducting Research (CASPER) East experiment (Wang et al., 2018) and MOST. These profiles are subsequently used to calculate modified refractivity vertical profiles. The Coupled Ocean-Atmosphere Mesoscale Prediction System (COAMPS®; Hodur, 1997) estimates modified refractivity profiles under the same conditions as COARE. Modeled profiles of wind speed, temperature, and specific humidity, for both COARE and COAMPS®, are used to calculate wind shear, NSSHG, and ASTD directly above the sea surface.

ii. Near-surface drivers of EDS found in (i) can be used to develop an empirical model to predict C_0 with reasonable accuracy based on a few basic *in-situ* measurements.

Relationships identified between C_0 and NSSHG based on hypothesis (i) for the COAMPS® dataset (i.e., the most densely populated dataset) are used to generate an empirical EDS model that predicts C_0, which then is used in the two-layer parametric refractivity model (Eqn. 7) to predict refractivity.

To evaluate the EDS model for reasonable accuracy, *in-situ* data collected during CASPER-East from a marine atmospheric profiling system (MAPS) are used. Residuals between MAPS (*in-situ*) refractivity (Wang et al., 2018) and that generated from the EDS model are computed within the "curvature zone" (i.e., 0.5m – $2Z_d$) to evaluate the EDS model. Shortcomings and limitations of the developed EDS model are identified based on this evaluation.

iii. PL predictions resulting from EDS model-based refractivity produce better comparisons with *in-situ* PL data then those based on alternative near surface refractivity estimation methods.

A parabolic equation propagation simulation is used to forward model PL patterns based-on M profiles calculated from various sources: calculated from the EDS model and alternative methods of estimating near surface refractivity such as MOST, linear extrapolation, and polynomial fits. All near surface estimation methods (including the EDS model) are blended into a MAPS measured profile, so the only difference between them occurs near the surface.

The sea surface is modeled in the propagation simulation to statistically replicate the ocean environment based on sea surface statistics during CASPER-East computed from wave spectra measured by deployed buoys; the modeled antenna set up in the propagation

simulation replicates that of *in-situ* radio frequency (RF) measurements. These simulated PL patterns are compared to *in-situ* X-band radar data that was also collected during CASPER-East. This radar data is comprised of measurements from four radar receivers, each with a unique altitude, measuring power as a research vessel sailed offshore/onshore from a transmitter at the end of a pier. Predicted and *in-situ* PL are compared using root mean-square-error (RMSE). Resulting PL RMSEs for EDS-based, and alternative methods of refractivity estimation are evaluated using a two-sample t-test, which determines if there is a statistically significant difference between the PL RMSEs for the EDS model relative to the other examined methods.

4.0 Methods

4.1 Data Sources

In-situ experimental and numerical data used within this study are discussed in subsections §4.1.1 and §4.1.2, respectively. The numerical data was sourced from a numerical weather prediction model and a semi empirical boundary layer model, which requires some *in-situ* data; these numerical data sets were evaluated for relationships between C_0 and thermodynamic properties. The relationship between C_0 and NSSHG is used to create an EDS prediction model that is evaluated using *in-situ* meteorological data. This model is subsequently used to extend *in-situ M* profiles to the surface; PL predictions based on refractivity estimated via the EDS model, along with conventional methods of estimating near surface refractivity, are compared to *in-situ* measured RF data described in section §4.1.1.

4.1.1 Experimental Data

The CASPER-East (Wang et al., 2018) experiment was performed to better understand radar wave propagation during ED conditions in the MASL; this experiment took place offshore Duck, North Carolina between 12 October and 3 November 2015. Meteorological data were collected from research vessels (*R/V*) *Atlantic Explorer* (*AE*) and *Sharp*, and from a small boat deployed from the *R/V Sharp*; an example overview of these data sources is shown in Figure 5 for 21 October 2015.

During the CASPER-East experiment, a weather balloon was outfitted with a MAPS that

included a radiosonde, which measured pressure, temperature, and relative humidity. It was deployed from a small boat launched from the *R/V Sharp* so the *R/V Sharp* would not contaminate measured vertical distributions of atmospheric variables near the surface (lowest ~10 m); the weather balloon was winched up and down ~7 times to obtain sufficient data to estimate mean modified refractivity over altitude as exemplified in Figure 6 (§2.2; Eqn. 4). A seventh order polynomial fit is used to estimate the mean *M* profile (i.e., MAPS polynomial *M* profiles; Rainer, 2016; Alappattu et al., 2016; Wang et al., 2018) from the data cluster as described in Wang et al. (2018) and shown in Figure 6; 36 MAPS polynomial *M* profiles were estimated from measured data over the course of the experiment for altitudes 0-60 m. A seventh order polynomial was used rather than a standard bin-averaged mean profile because it enabled retention of larger near-surface gradients (Alappattu et al., 2016; Rainer, 2016; Wang et al., 2018). Examples of times and locations of MAPS datasets for 21 October 2015 are shown in Figure 5.

Bulk environmental data utilized in this study includes air temperature, pressure, wind speed, and specific humidity, which were measured from the *R/V Sharp's* bow mast (denoted by COARE symbols in Figure 5) by sensors that were mounted 12 meters above the sea surface and sampled continuously at 20 Hz; a mean for each property was calculated every 30 minutes (Wang et al., 2018). Sea surface temperature (SST) measurements are bulk measurements taken from the *R/V Sharp* water intake (Alappattu et al., 2017), which are averaged over 5-minute intervals (Wang et al., 2018), and corrected using an infrared SST autonomous radiometer skin temperature probe.

Sea state measurements, specifically significant wave height and sea surface peak wavenumber, were obtained from a transect of moored wave buoys (Figure 5) stationed off

Duck, North Carolina during CASPER-East (Wang et al., 2018). The buoys measured wave spectra every 30 minutes and power spectral densities of all 5 buoys for each measurement time were averaged to estimate a spatial-mean power spectral density to correspond to each *R/V Sharp* bow mast measurement (Pastore et al., 2021; Pastore et al., 2022). Significant wave height (h_s) was calculated from mean power spectral density by:

$$h_s = 4\sqrt{m} \tag{8}$$

where m is the integral of mean power spectral density. Peak wavenumber is the wavenumber associated with the highest mean power spectral density.

During the CASPER-East experiment, *in-situ* EM RF "ship-to-shore" propagation data were collected using four receivers on the A-frame of the *R/V AE* at altitudes of 4.0 m, 6.0 m, 9.2 m, and 12.3 m, and the transmitter was located on Duck Pier at a range of altitudes spanning 10.3 m to 11.1 m due to tidal fluctuations. RF data were collected at 10.7 GHz frequency with vertical polarization over ranges up to 60km as the *R/V AE* sailed offshore (Figure 5) away from the shore transmitter. Quality controlled (Wang et al., 2019; Pastore et al., 2022) ship-to-shore datasets that were collected within 24 hours of the MAPS balloon deployments are used within this study (8 radar datasets). Wang et al. (2019) and Pastore et al. (2022) provide further information on collection and quality control of the RF dataset.

4.1.2 Numerical Data

The COARE 3.0 algorithm (Fairall et al., 1996; Fairall et al., 2003) is a semi-empirical boundary layer model that uses MOST to estimate mean near-surface wind ($\overline{U}$), temperature ($\overline{T}$), and specific humidity vertical profiles ($\overline{q}$) using bulk atmospheric and sea state measurements (Fairall et al., 1996; Fairall et al., 2003). MOST $\overline{U}$, $\overline{T}$, and $\overline{q}$ profiles are respectively (Fairall et al., 2003):

$$\bar{U}(z) = U_s + \frac{U_*}{k}\left(\ln\left(\frac{z}{z_o}\right) - \psi_U\left(\frac{z}{L}\right)\right) \quad (9)$$

$$\bar{T}(z) = T_s + \frac{T_*}{k}\left(\ln\left(\frac{z}{z_{oT}}\right) - \psi_T\left(\frac{z}{L}\right)\right) \quad (10)$$

$$\bar{q}(z) = q_s + \frac{q_*}{k}\left(\ln\left(\frac{z}{z_{oq}}\right) - \psi_q\left(\frac{z}{L}\right)\right) \quad (11)$$

where U_s is ocean surface current, T_s is skin SST, q_s is surface saturation specific humidity, k is the von Karman constant (0.4), z_{oT}, and z_{oq} are roughness lengths for wind, temperature, and specific humidity respectively, U_*, T_*, and q_* are scaling factors for wind, temperature, and specific humidity respectively, and L is MO length. ψ functions are the integrated forms of the universal stability functions for wind, temperature, and humidity denoted by subscripts *U*, *T*, and *q*, respectively, that have been empirically determined (Businger et al., 1971). Equations (9)-(11) are the integrated forms of the universal functions for temperature, humidity, and wind. The Appendix provides these universal functions.

Bulk environmental estimates used in COARE include previously described temperature, wind, and specific humidity measurements sourced off the bow mast of the *R/V Sharp,* SST, and sea state parameters (§4.1.1), which are used to determine scaling factors and the MO length scale (Fairall et al., 2003). Figure 7A and 7B show *in-situ* atmospheric and SST measurements from the *R/V Sharp* that are used in the COARE 3.0 algorithm (Fairall et al., 1996; Fairall et al., 2003) to estimate vertical profiles of wind, temperature, and humidity. Figure 7C shows the estimated thermodynamic regimes associated with the same time period; when ASTD, i.e., the difference between the measured temperature at 12m and the measured skin SST as seen in Figure 7A and 7C, is negative the atmosphere is unstable, which was observed for most of CASPER-East. Surface specific humidity was estimated

from the measured skin SST, the measured sea level pressure, and an assumption of 98% relative humidity at the sea surface (Peixoto and Oort, 1996; Ross and Elliott,1996; Buck 1981). The conversion of relative humidity to specific humidity was calculated (Peixoto and Oort, 1996; Ross and Elliott,1996; Buck 1981):

$$e_s = f6.112\exp\left[\frac{(18.279 - T_s/227.3)T_s}{T_s + 257.87}\right] \quad (12)$$

$$f = 1.0007 + 3.46p(10^{-6}) \quad (13)$$

$$R_H = 100\frac{e}{e_s} \quad (14)$$

$$q = \frac{0.622e}{p - 0.378e} \quad (15)$$

where f is a correction to account for the difference in pressure due to a mixture of vapor and air over water. T_s is skin SST in Celsius, e_s is saturation vapor pressure in Pascals, and R_H is relative humidity. Note, pressure must be in units of millibars, and partial vapor pressures must be in units of Pascals. Note that slightly different forms of these conversion equations exist with minor variations on the empirical constants (Elliot and Gaffen, 1991). Significant wave height and peak wavenumber calculated from the buoy data (§4.1.1) are used to calculate the roughness length for the wind, temperature, and specific humidity (z_o, z_{oT}, and z_{oq}). Figure 8 shows example COARE wind, temperature, and specific humidity profiles for 17 October 2015 at 00:12:29 UTC (Eqns. 9, 10, and 11), of which, temperature and specific humidity are used to calculate modified refractivity (Figure 8D) using Eqns. 4 and 5.

COAMPS® (Hodur, 1997) is a numerical weather prediction model that predicts mesoscale atmospheric properties. Initial boundary conditions used in COAMPS® for the

atmosphere and ocean are estimated from the Naval Global Environmental Model (Hogan et al., 2014) and the Global Hybrid Coordinate Ocean Model (Halliwell et al., 2004), respectively. COAMPS® has a resolution of seventy-one levels between 4m-4000m, only 6 levels are below 100m and therefore within the MASL. This resolution is unable to resolve EDs, so low altitude COAMPS® data is blended with the Navy Atmospheric Vertical Surface Layer Model (NAVSLaM, Fredrickson, 2015), which, like COARE, uses MOST to characterize near-surface atmospheric property vertical profiles. The resolution of the blended vertical forecasts is a decimeter and spans the sea surface to 100m in altitude. COAMPS® data consists of one forecast per hour over the duration of the CASPER-East experiment (a total of 648 forecasts). Each forecast includes vertical profiles of temperature, specific humidity, and modified refractivity at 31 geographical locations ~2km apart over a 60km offshore transect beginning at Duck Pier, NC; this spatiotemporal resolution is visualized in Figure 5 as the nodes of the grid. Figure 9 shows an example of *M* profiles from a COAMPS® forecast on 10 October 2015 at 0600.

4.2 Data Analysis

4.2.1 Analyzing Near Surface Drivers of EDS

To parameterize COARE and COAMPS® *M* profiles, a nonlinear least squares regression, which minimizes the sum of the squares of the residuals between the parametric model and numerical data, is applied. The parametric model is described by Eqn. 7 and two model parameters, ED curvature (C_0) and mixed layered slope (m_1) are fit. Other model parameters, EDH (Z_d) and surface modified refractivity (M_0), are estimated directly from COARE and COAMPS® *M* profiles. M_0 is the surface refractivity of the respective COARE or COAMPS® refractivity profile, and EDH is determined as the altitude where

the gradient of modified refractivity $\left(\frac{\partial M}{\partial z}\right)$ changes sign (from negative to positive). Figure 10 shows an example of a nonlinear least square regression fit to a COAMPS® profile, where agreement between the two profiles is evident.

Mean squared error (MSE; E_r) of refractivity is used to evaluate the goodness of fit:

$$E_r = \frac{1}{n_{mref}} \sum_{i=1}^{n_{mref}} \left(M_{c_i} - \widehat{M}_i\right)^2 \tag{16}$$

where M_c is the COARE/COAMPS® M profiles, $\widehat{M}$ is modified refractivity estimated from the parametric model (Eqn. 7), and n_{mref} is the number of points in the modified refractivity profile between the surface and $2Z_d$.

Only profiles that contain an ED and fit the parametric model well are considered in this study (E_r < 1 M-Unit^2). This restriction leaves ~74% of the COARE profiles and ~83% of the COAMPS® profiles available for subsequent analysis (Figure 11). This tight criterion ensures that interpretations of results linking NSSHG, ASTD, and wind shear to C_0 cannot be attributed to errors stemming from the parametric model not being able to adequately fit the M profile.

Estimated C_0 from a nonlinear least square regression fits are used to evaluate relationships between C_0 and NSSHG, wind shear, and ASTD to determine a predictive relationship between C_0 and these environmental variables. For both COARE and COAMPS®, ASTD is calculated by subtracting skin SST from air-temperature predictions at z=$2Z_d$. For both COARE and COAMPS®, NSSHG (Ψ_s) and wind shear are calculated by finding the slope of specific humidity or wind speed with altitude, respectively, estimated between the points at z=0 m and that at z=$2Z_d$. This altitude range is chosen to ensure these gradients envelop variations spanning the surface into the constant flux layer.

4.2.2 EDS Prediction Model

Linear relationships between C_0 and NSSHG, wind shear, and ASTD were evaluated using statistical analysis such as the coefficient of determination and correlation coefficient. The relationship between C_0 and the thermodynamic property with the highest correlation, NSSHG, is fit to a linear function, which relates this thermodynamic parameter to C_0:

$$C_0 = \alpha \Psi_s + C_{0y} \tag{17}$$

C_{0y} is the y-intercept and α is the slope of the linear fit. C_0 predicted via Eqn. 17 is subsequently used in the two-layer refractivity model (Penton and Hackett, 2018; Eqn. 7) to estimate a refractivity profile using a known surface refractivity, duct height, and mixed layer slope; this approach will be henceforth referred to as the EDS model. This implementation of the EDS model uses the Penton and Hackett (2018) two-layer refractivity model but any parametric model utilizing the C_0 parameter could be implemented instead.

The EDS model is verified using the MAPS data (see §4.1.1); only MAPS polynomial *M* profiles containing EDs are used (~92% of the aforementioned 36 datasets). MAPS polynomial *M* profiles (§4.1.1) are used for the validation and comparison because this dataset was not utilized in generating the EDS model and do not necessarily have MOST-like behavior built-into them.

To calculate the NSSHG for the MAPS dataset, surface values of specific humidity are estimated using skin SST obtained from the *R/V Sharp*, an assumption of 98% relative humidity at the surface (Peixoto and Oort, 1996; Ross and Elliott,1996; Buck 1981), and Eqns. 12-15, whereas the specific humidity at $z=2Z_d$ is that estimated by the MAPS polynomial. This estimate of the surface value is used rather than using the extrapolation

of the polynomial fit because the MAPS polynomial specific humidity profiles can lack accurate steep near surface gradients (Wang et al., 2018; Pastore et al., 2021).

To estimate *M* profiles, the predicted C_0 is used within the two-layer refractivity model (Eqn. 7; §2.3) along with M_0 and Z_d from the MAPS polynomial *M* profile. Comparisons between refractivity based-on the EDS model and that of the MAPS polynomial *M* profiles are performed in the curvature zone, defined as $z = 0.5\text{m} - 2Z_d$, to evaluate the EDS method for reasonable accuracy. The curvature zone is not impacted by m_1 and therefore discrepancies are only attributable to C_0.

Note, residuals are not calculated below 0.5m so they are not skewed by discrepancies in steep near surface refractivity gradients between MAPS polynomial *M* profiles and EDS model profiles. Due to the large scatter in the *in-situ* measurements used to develop the MAPS polynomial *M* profiles, and therefore the need to fit these data with a polynomial function, inaccuracies in the lowest altitudes where measurements were sparse to non-existent due to practical and technical limitations of the sampling equipment could exist. This shortcoming implies that discrepancies between the EDS model and the MAPS polynomial in this region may not be completely attributable to limitations of the EDS model and may also have to do with limitations of MAPS polynomial fit. To mitigate this issue, the profiles are only compared within the "curvature zone."

To calculate residuals, the EDS profile was first shifted by a constant (therefore not influencing the refractive gradients) of modified refractivity such that modified refractivity at the EDH of each profile was equivalent. These residuals in the curvature zone are most representative for isolating EDS differences.

Notably, to use the EDS method to extend *in-situ* data to the surface *a priori* estimates of

EDH and M_0 are required. Using the EDS method at altitudes above the evaporation layer would require estimation of m_1 as well.

4.2.3 EDS Refractivity and Propagation Comparisons

Henceforth, only MAPS polynomial *M* profiles collected within 24 hours of an *in-situ* PL measurement are used (~56% of MAPS polynomial *M* profiles). *M* profiles extended to the surface using the EDS model are compared against three conventional techniques of estimating near surface refractivity: linear and non-linear extrapolation, and MOST. The linearly extrapolated profiles are MAPS polynomial *M* profiles extrapolated to the surface from 3 m, as this height range is considered a region where vessel contamination of measurements is highly likely and satisfies resolution requirements discussed in Thews (1990). The non-linear extrapolation is the MAPS polynomial fit profiles (Rainer, 2016; Alappattu et al., 2016; Wang et al., 2018); this near surface estimation method fits an *in-situ* data cloud that does not have a clear "cut-off" altitude yet utilizes scarce scattered near surface measurements to estimate a mean *M* profile. MOST profiles are calculated using COARE and environmental parameters estimated by the MAPS data collection (§4.1.1).

EDS and MOST *M* profiles are blended into the MAPS polynomial *M* profiles using a weighted average over the altitude range: Z_d - Z_d + 3 m. The blended profiles are 100% the near surface estimation method (i.e., EDS or MOST) from the surface to Z_d and 100% the MAPS polynomial *M* profiles 3m above the EDH (Figure 12). Thus, the only differences between *M* profiles occurs below $z = Z_d + 3$ m where near surface gradients differ. Figure 13 shows an example of a blended profile for the EDS model.

To compare methods of estimating *M* profiles near the surface with respect to their use in propagation modeling, RMSEs are calculated between *in-situ* measured PL and simulated

PL of blended EDS and conventional methods profiles. The Variable Terrain Radio Parabolic Equation (VTRPE) computer model (Ryan, 1991) is used to simulate EM waves in varying environmental conditions within the MASL and accounts for environmental effects (i.e., reflection and refraction). The simulated antenna set up in VTRPE is matched to that of the *in-situ* RF data collection previously described in §4.1.1. VTRPE models EM wave propagation over rough surfaces; sea surface realization in VTRPE is based on a modified Donelan-Pierson-Banner spectral wind-capillary wave model (Pierson and Moskowitz, 1964; Donelan et al., 1985; Banner et al., 1989) that is appended to a narrow-band Gaussian swell model. To match *in-situ* wave conditions, parameters of said model are adjusted so the modeled wave spectrum matches the averaged buoy spectrum described in §4.1.1 (Figure 5).

RMSE (Ω) between the simulated and *in-situ* PL are calculated:

$$\Omega = \sqrt{\frac{1}{n_{prop}} \sum (R^m - R^s)^2} \tag{18}$$

where R^S is simulated PL, R^m is measured PL, and n_{prop} is the number of propagation measurements over all ranges beyond 13 km at all 4 receiver heights. To minimize the impact of slight differences in multipath "null" locations on the RMSE statistic, PL predictions and measurements were averaged over the peak sea surface wavelength (Penton and Hackett, 2018) before the RMSE is computed. Furthermore, results are focused on PL beyond 13 km – referred to as "long range" since this region is mostly beyond the multipath nulls. Figure 14 shows an example of simulated PL for a MAPS polynomial profile with the *in-situ* radar receiver heights denoted as horizontal lines (§4.1.1).

RMSEs for the various methods (Ω) are compared utilizing two-sample t-tests to establish

if the mean RMSE for each conventional method is significantly different from the EDS model's mean RMSE. This method can only be used if the data is known or assumed to be normally distributed (i.e., mean and median are approximately equivalent) and each population is independent. This test is performed three times; for each test, RMSEs of the EDS profiles are the first population and RMSEs of each conventional method (i.e., linear extrapolation, MAPS polynomial *M* profiles and MOST blended at EDH) are the second population. The t-test is performed by first calculating the t-statistic (*t*):

$$t = \frac{\overline{\Omega_{M1}} - \overline{\Omega_{M2}}}{\sqrt{\frac{S_{M1}^2}{C_{Mref}} + \frac{S_{M2}^2}{C_{Mref}}}} \tag{19}$$

where $\overline{\Omega_{M1}}$ and $\overline{\Omega_{M2}}$ are the mean RMSE for the EDS method and other compared method (i.e., linear extrapolation, MAPS polynomial *M* Profiles, or MOST profiles), respectively, S_{M1} and S_{M2} are their respective standard deviations, and C_{Mref} is the number of compared *M* profiles.

Degrees of freedom (d_f) are the number of independent measurements able to vary: $d_f = 2C_{Mref} - 2.$; for this study, $d_f = 38$. Significance level is the probability of the null hypothesis being rejected, despite being true; for this study, the significance level was 5%. Degrees of freedom and significance level are used to find the critical value of a t-probability density function. The critical value is the threshold for the area under the probability distribution curve to be equal to the significance level and accounts for the sampled data's uncertainty; therefore, if the absolute value of *t* is less than the critical value, it is not significant since it is within the margin of error and indicates there is not enough evidence to reject the null hypothesis, i.e., there is no difference between mean RMSE of each tested method. If the resulting absolute value of *t* is greater than the critical value, the null hypothesis is rejected.

If the null hypothesis is rejected, that establishes there is a significant difference between the RMSEs of the two tested methods and presumably the one with lower mean RMSE better replicates *in-situ* PL data.

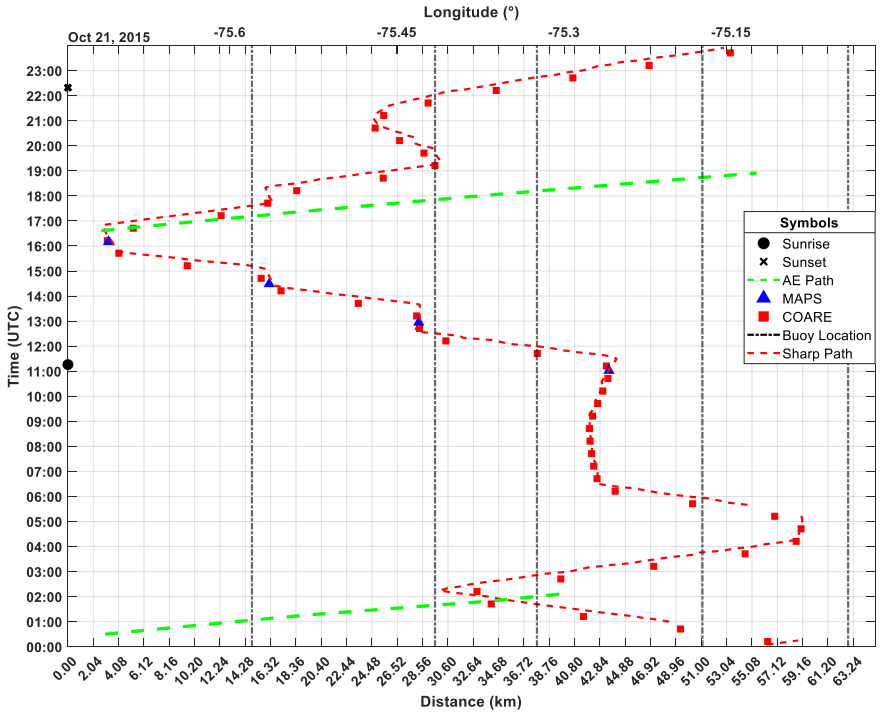

Figure 5. Example spatial and temporal map of data collection on 21 October 2015. The bottom x-axis represents the distance in km from Duck Pier, whereas the y-axis represents the time the data was collected in UTC. The green lines represent the tracks of the R/V AE during radar data collection, the black symbols represent sunrise and sunset, the vertical dot-dash black lines represent the buoy locations, the red squares represent the times and locations where 30-min averaged meteorological data were collected from the R/V Sharp bow mast that is used by the COARE algorithm, and the blue triangles represent the times and locations the MAPS system was winched up and down from a small boat deployed from the R/V Sharp to obtain the data for the 7th order polynomial fits. The nodes of the grid represent the spatiotemporal resolution of the blended COAMPS®-NAVSLaM predictions.

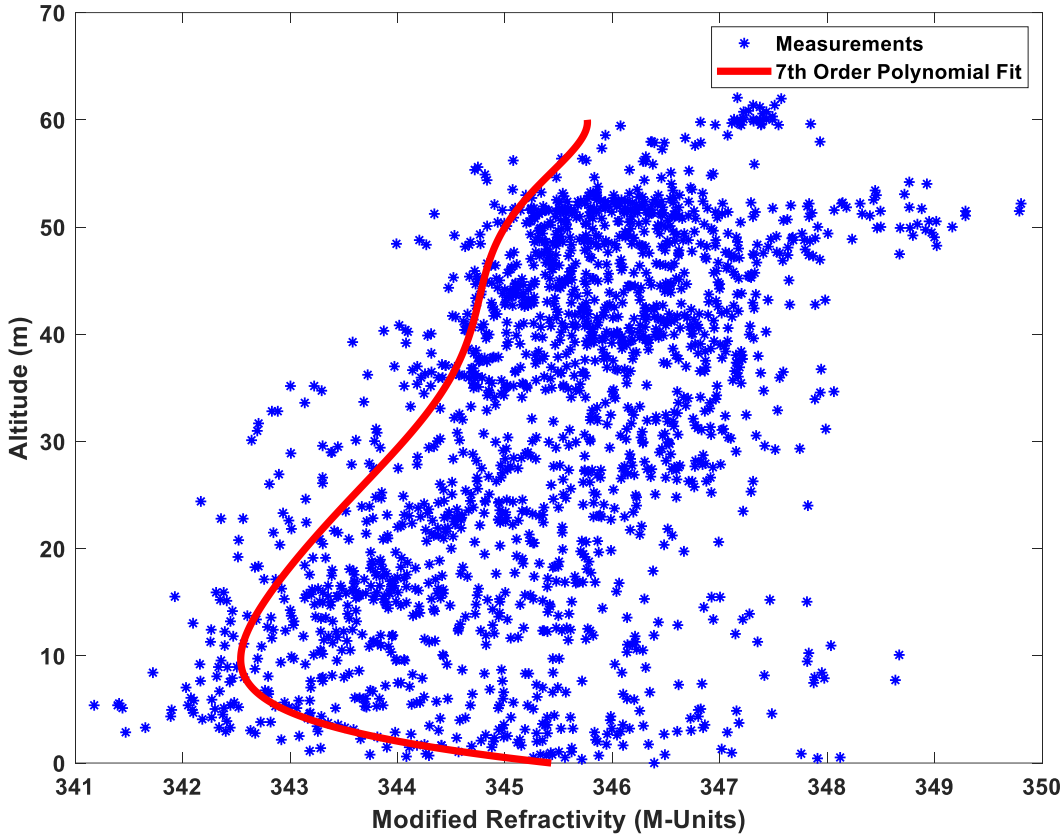

Figure 6. Measured modified refractivity, blue stars, calculated from the in-situ tethered balloon measurements of temperature, pressure, and humidity. The red line is the seventh order polynomial fit to the cluster of modified refractivity data points as described in Alappattu et al. (2016), Rainer (2016) and Wang et al. (2018).

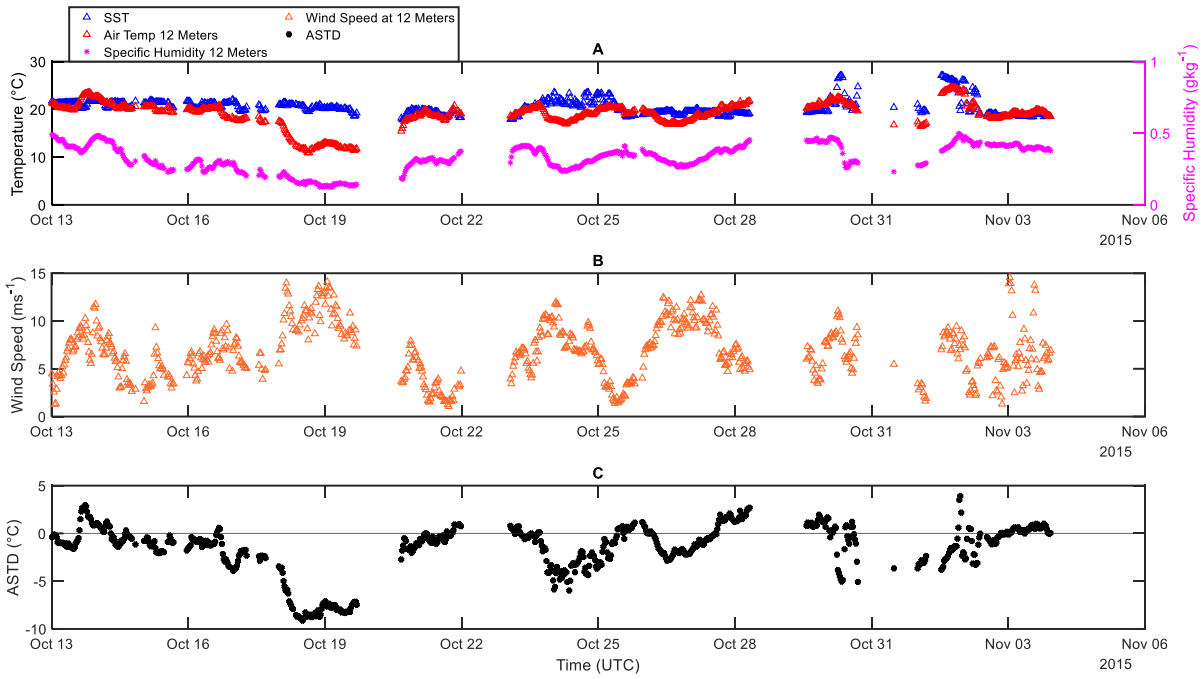

Figure 7. (A) In-situ measurements (Wang et al., 2018) used in the COARE algorithm to compute atmospheric vertical profiles of temperature and specific humidity: skin sea surface temperature (SST), and air temperature and specific humidity at 12 meters above the sea surface measured from the bow of the R/V Sharp. (B) In-situ measurements (Wang et al., 2018) of wind speed at 12 meters above the sea surface measured on the bow of the R/V Sharp also used in the COARE algorithm to calculate atmospheric vertical profiles of wind speed. (C) Air-sea temperature difference (ASTD) used to estimate the thermodynamic stability regime of the atmosphere.

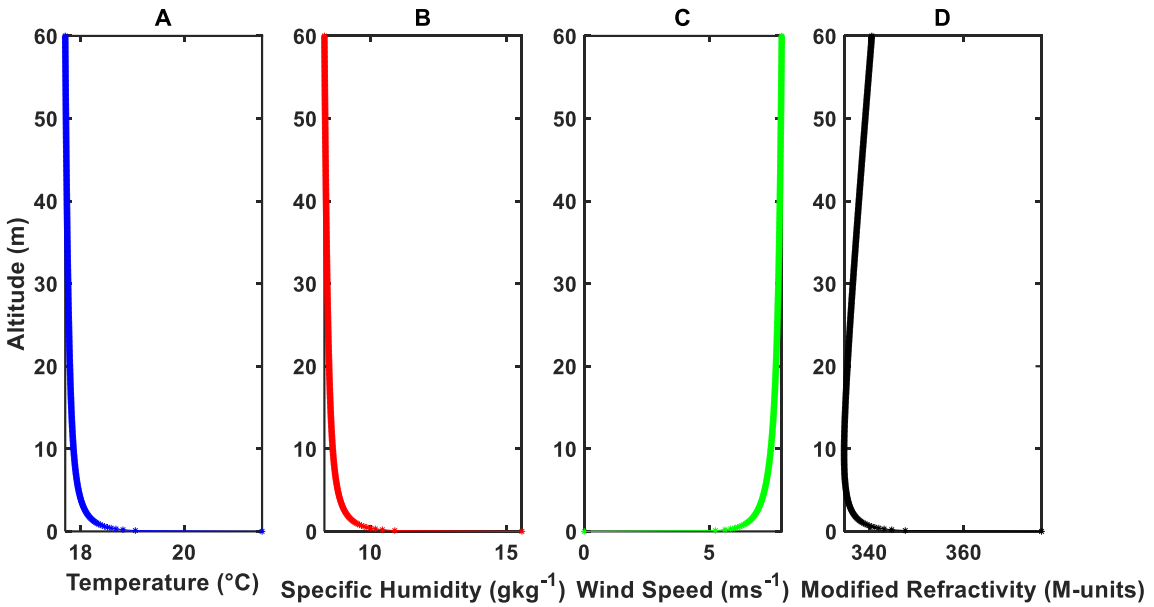

Figure 8. COARE vertical profiles from 17 October 2015, at 00:12:29 UTC of (A) temperature, (B) specific humidity, and (C) wind speed. (D) The corresponding modified refractivity profile calculated using the measured pressure at 12m from the R/V Sharp, (A) temperature, (B) specific humidity, and Eqns. 4 and 5.

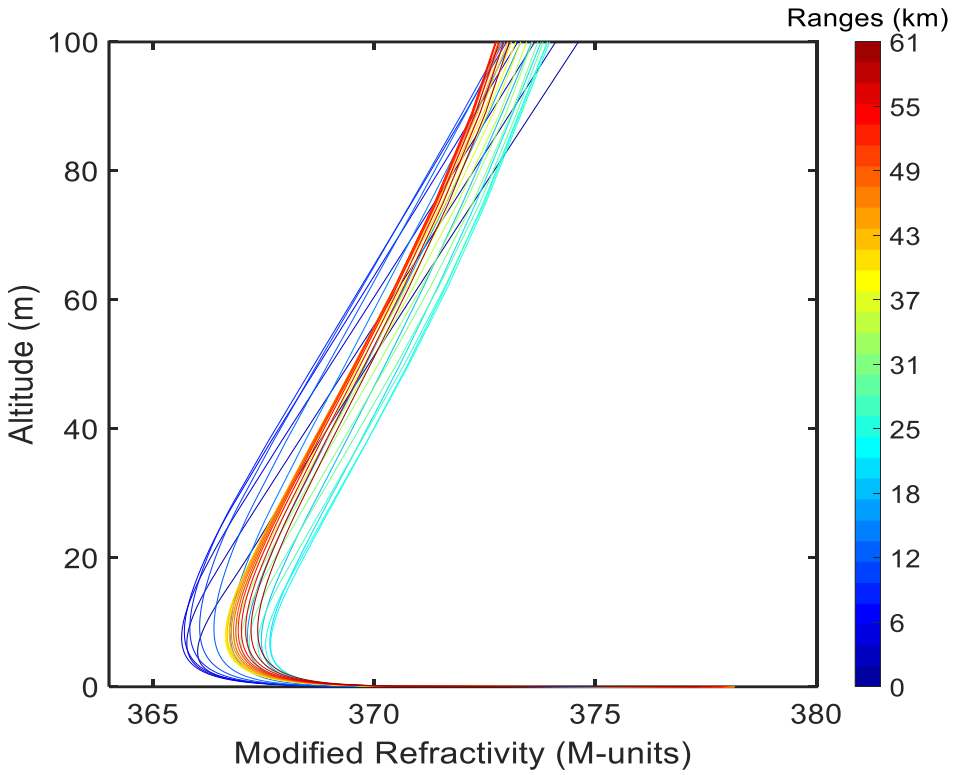

Figure 9. Modified refractivity profiles from a COAMPS®-NAVSLaM blended forecast corresponding to 10 October 0600Z, color denotes their respective ranges (km) (see colorbar).

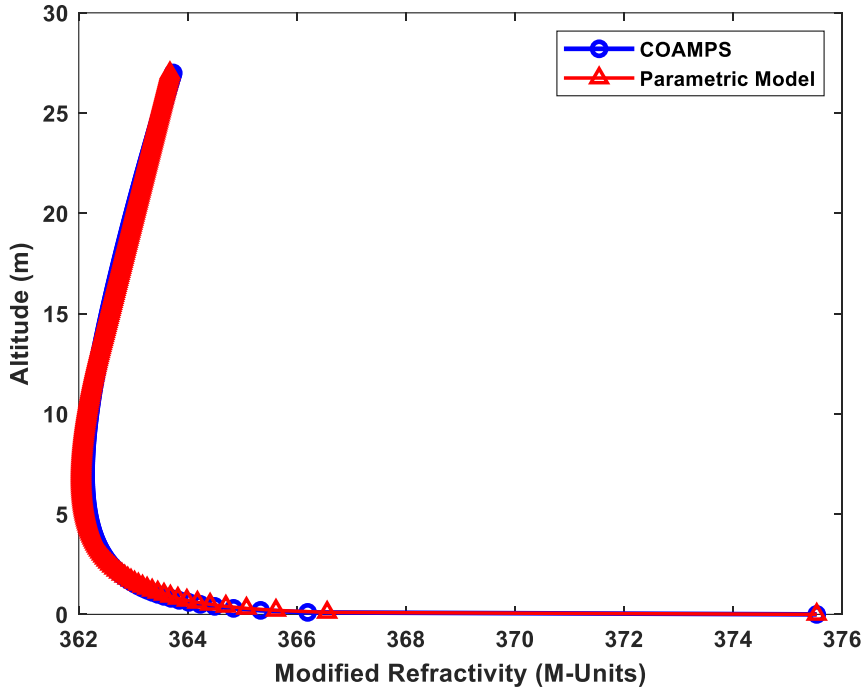

Figure 10. Example nonlinear least squares regression fit of Eqn. (7) to a COAMPS® modified refractivity profile. The blue line represents COAMPS®, and the red line represents the parametric model (Eqn. 7) for 28 October 0500z.

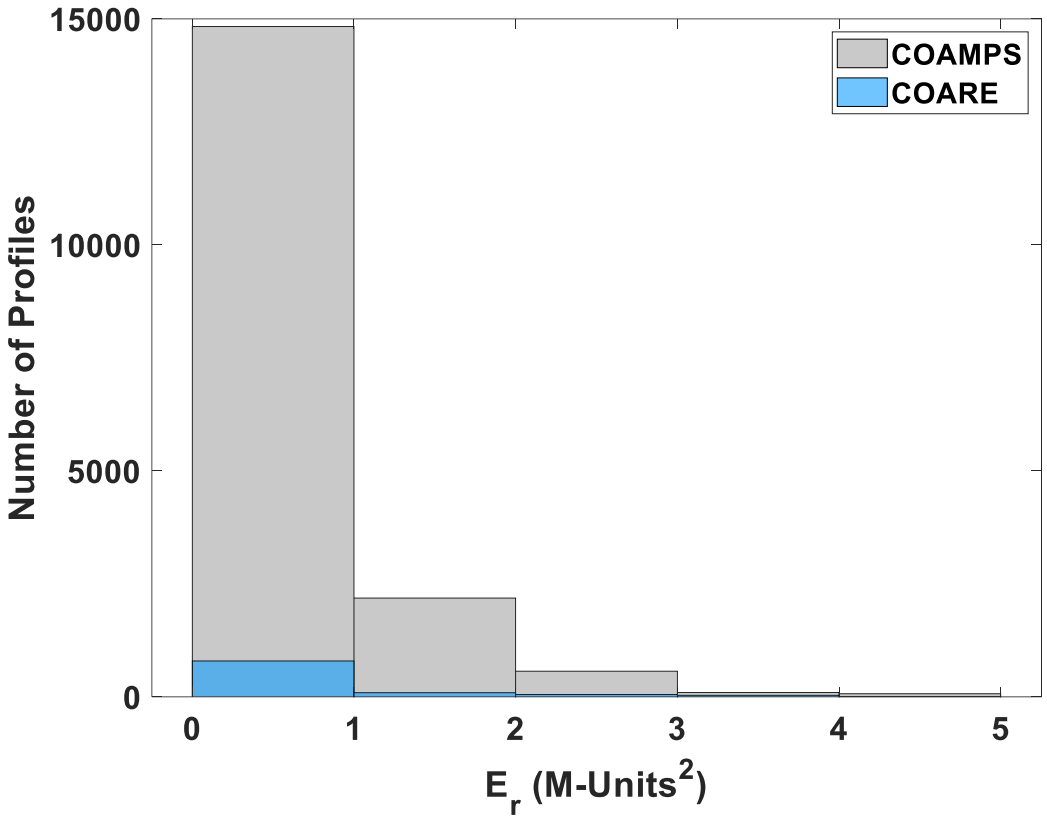

Figure 11. Histograms of E_r for COAMPS® (grey) and COARE (blue), where only the fits with $E_r < 1$ M-units^2 are used in this study.

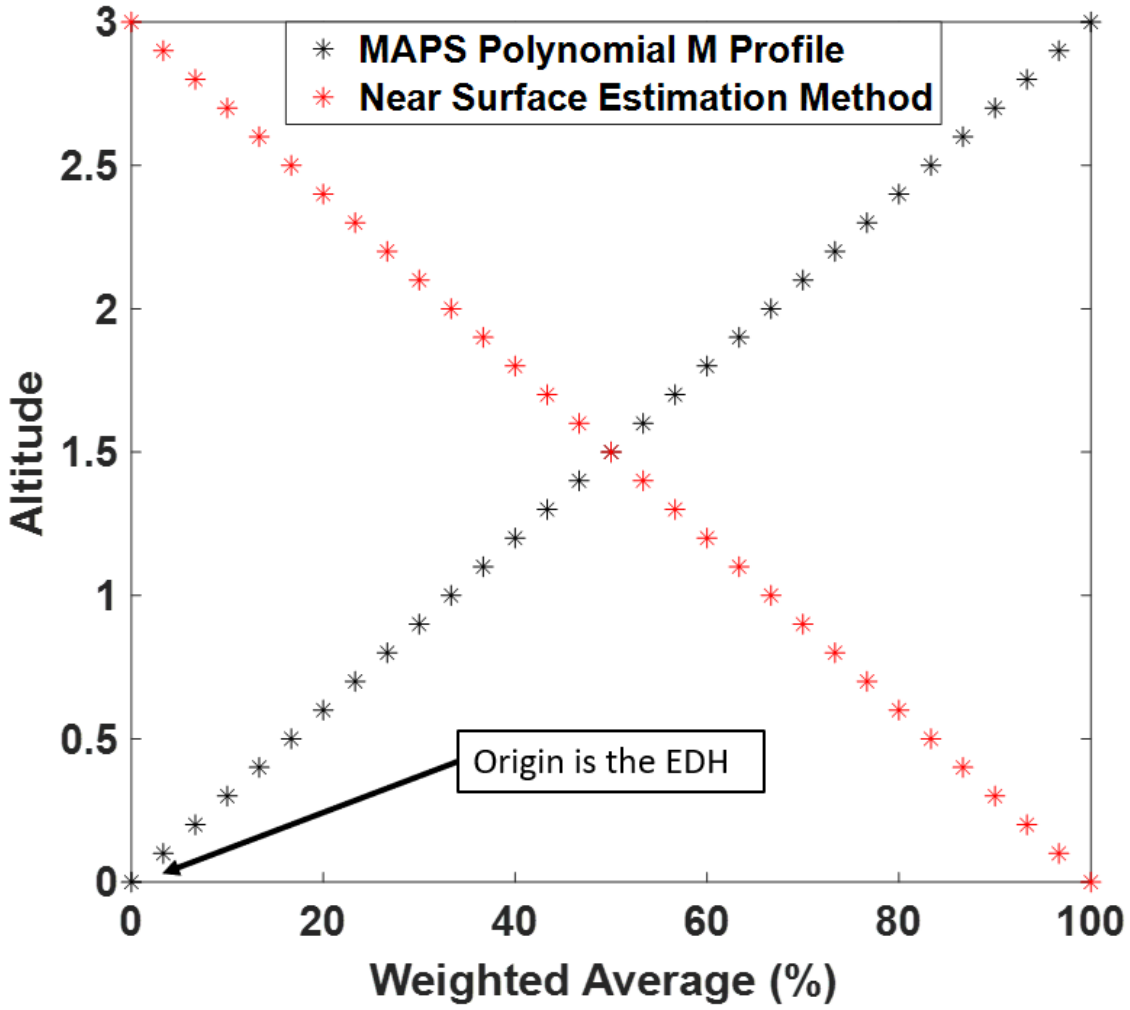

Figure 12. The weighted average percent over the blending range (i.e., Z_d to Z_d + 3m) for the EDS or MOST profile that is blended with the corresponding MAPS polynomial M profile.

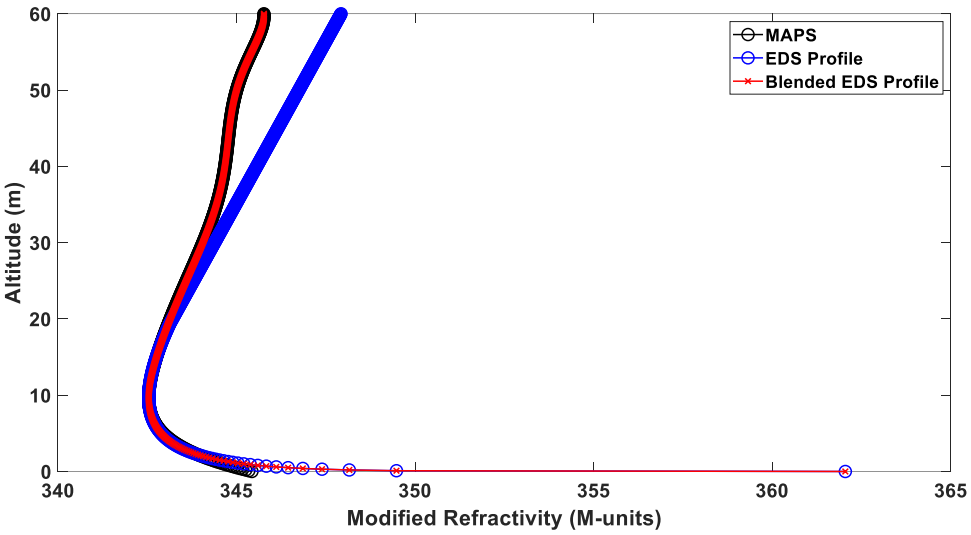

Figure 13. Example EDS model estimated profile blended into a MAPS polynomial profile for 13-Oct-2015 16:49:05 with an EDH of 9.7 m.

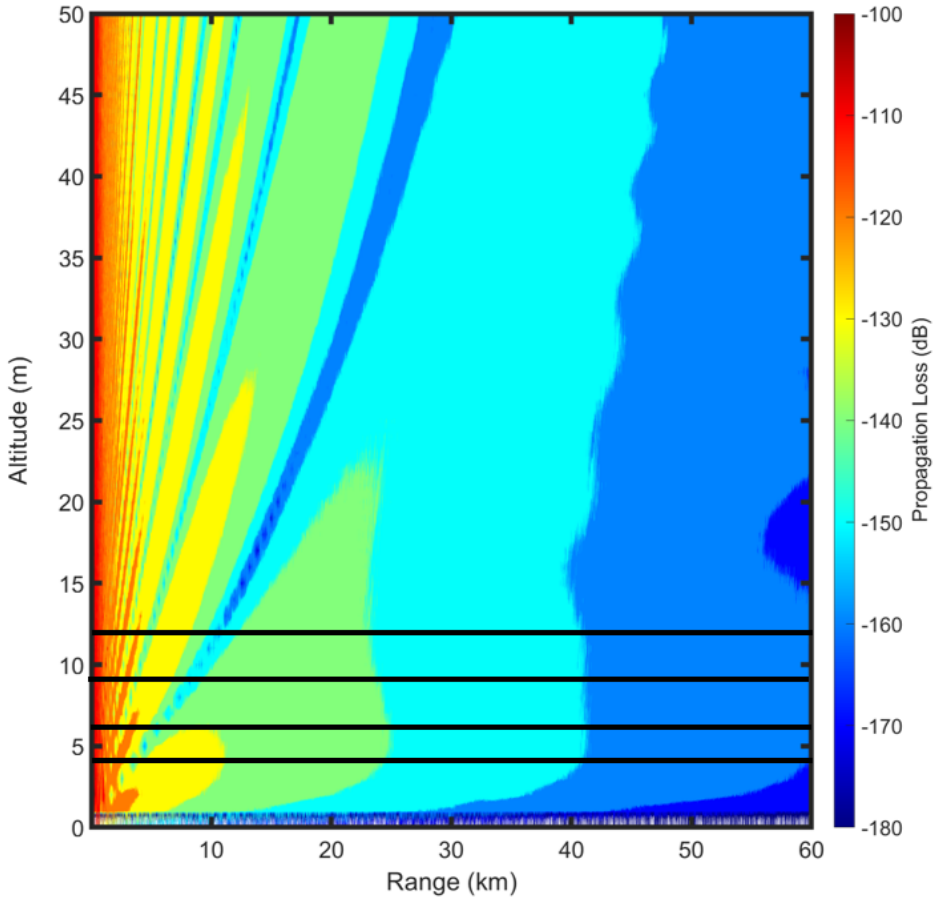

Figure 14. VTRPE simulated propagation loss for 21 October MAPS polynomial M profile collected at 14:29:07 UTC. The black horizontal lines represent the heights of the in-situ radar receivers located at 4 m, 6 m, 9 m, and 12 m.

5.0 Results

The validity of using the parameter C_0 as an estimation of profile curvature is discussed in the first subsection (§5.1) and relationships between C_0 and thermodynamic gradients (i.e., ASTD and NSSHG) as well as with wind shear are discussed in subsection §5.2. The third subsection explores an EDS model (§5.3). The EDS model is used to estimate C_0 under the same environmental conditions as 33 MAPS refractivity profiles (Wang et al., 2018) and the curvature of these EDS-based refractivity profiles are compared against the MAPS polynomial *M* profiles. Simulated PL based-on EDS modeled profiles and other near surface refractivity estimation methods are compared to *in-situ* PL data to explore potential applicability of the developed EDS model for propagation modeling in the final subsection (§5.4).

5.1 Evaporation Duct Shape Metric

The metric used to describe EDS is C_0 from the two-layer refractivity model (Eqn. 7) proposed by Penton and Hackett (2018) and Matsko and Hackett (2019). To verify this metric, the relationship between C_0 and average second order derivative of modified refractivity with altitude (ASOD; $\overline{\frac{\partial^2 M}{\partial z^2}}$) is shown in Figure 15. Pastore et al. (2021) use ASOD as a measure of duct curvature because the ASOD is an indicator of the shape of a function. In general, the relationship between ASOD and C_0 is linear with a statistically signigficant correlation coefficient of 0.70 and p-value of zero (Figure 15A). This correlation increases when correlating ASOD and C_0 for refractivity profiles with similar

duct heights (Figure 15B); for example the correlation coefficient for profiles with ~10m EDH is 0.99. The correlation coefficient increases when only considering one EDH (e.g., ~10m, Figure 15B) because EDH also influences the curvature of the ED. When the effects of EDH on curvature are removed by isolating a narrow duct height range, the relationship between duct shape and C_0 is more evident. This result reinforces that C_0 is a model parameter that can change the ED shape without changing the duct height (Saeger et al., 2015; Penton and Hackett, 2018). Due to these results, C_0 is considered a valid metric of refractivity profile curvature or shape. C_0 is used as the shape metric instead of the ASOD directly because of its applicability in logarithmic-linear models used in propagation simulations.

5.2 Near Surface Drivers of EDS

Fundamentally, thermodynamic properties such as ASTD and NSSHG influence modified refractivity (§2.2, Eqn. 4), thus it is logical to conclude that EDS is dependent on gradients of these thermodynamic properties. Wind shear is a flow characteristic that can destroy vertical gradients of these thermodynamic properties. Relationships between ASTD, NSSHG, wind shear and C_0 are explored.

EDs are generally permanent features over marine surfaces in unstable thermal regimes, yet, rare in stable thermal regimes due to presumably weaker near surface thermodynamic gradients (Skolnik, 2003); thus, atmospheric stability is an important property to consider when evaluating EDs. For example, Ding et al. (2020) demonstrated modeled EDHs have high sensitivity to thermodynamic stability functions used within various models in their study. To explore relationships between C_0 and stability, the ASTD is utilized because it is a simple metric of stability.

Figure 16 illustrates a weak inverse relationship between C_0 and ASTD for both COARE and COAMPS® profiles (Table 1); notably, scatter in the data is reduced near expected neutral values (i.e., ASTD of 0 °C and C_0 = 0.125 M-Units m^{-1}) with a slight offset. In stable regimes (i.e., ASTD > 0°C), C_0 values are smaller (<~0.2 M-Units m^{-1}) whereas in unstable regimes (i.e., ASTD < 0°C), C_0 values are larger (>~0.2 M-Units m^{-1}) (Figure 16). There is a subset of COARE and COAMPS® profiles with C_0 between ~0.35 and 0.55 M-Units m^{-1} that are associated with an extremely unstable thermal regime (i.e., ASTD < -6°C) and do not follow the trend of near neutral or mildly unstable profiles. This highly unstable regime, at or near convective conditions, likely invokes slightly different forms of the stability functions between NAVSLaM and COARE (Fredrickson, 2016) since this regime exhibits the least overlap in the COARE and COAMPS® predictions. In this stability regime, the seemingly different relationship between C_0 and ASTD could suggest that other factors are significant.

Near surface wind speeds could influence ED properties by mixing thermodynamic gradients responsible for controlling atmospheric refractivity (Bean and Dutton, 1968; Eqn. 4). For example, McKeon (2013) found relative humidity and temperature weakly influence EDH in times of increased wind speeds. As such, the relationship between C_0 and wind shear is investigated directly above the marine surface to provide a more holistic picture of what processes drive variations in C_0 with respect to ASTD, as shown in Figure 17. Notably, COARE and COAMPS® behave similarly with respect to wind shear and NSSHG so they are shown using the same symbols to focus on only the overall trends between C_0 and the respective thermodynamic property.

When wind shear is smaller (~ < 1 s^{-1}), the range of potential C_0 values is large (Figure 17)

and C_0 is generally below 0.2 M-units m^{-1} during times of greater wind shear (~ > 1 s^{-1}). In slightly unstable conditions and low wind shear, C_0 is a strong function of wind shear with much higher C_0 occurring during times of lower wind shear. This observation could be attributed to growing instabilities due to steeper near surface thermodynamic gradients in comparison to times with larger wind shear where those gradients are mixed by the wind. In near neutral to stable conditions, wind shear varied up to 3 s^{-1} (Figure 17), which C_0 was relatively insensitive to, remaining at small values (~ 0 – 0.1 M-Units m^{-1}) regardless of wind shear. This observation is potentially due to mechanical mixing which limits stability causing thermodynamic gradients to remain approximately the same regardless of wind shear – at least over the range measured here. Notably, Figure 17 shows the very unstable (near convective) cluster of M profiles seen in Figure 16 as occurring during a relatively low wind shear of ~0.5 s^{-1}.

The final driver of ED characteristics this study evaluates is NSSHG due to ED's forming from steep near surface humidity gradients (Skolnik, 2003, Karimian et al., 2013). Pastore et al. (2021) suggest stability regime and near surface humidity gradients are likely direct drivers of EDS (i.e., duct curvature or in this study C_0). This study utilizes specific humidity because it is not influenced by temperature or pressure.

Figure 18 illustrates the relationship between NSSHG and C_0 with respect to ASTD; COARE and COAMPS® both have a strong inverse linear relationship between C_0 and NSSHG implying NSSHG is a primary driver of C_0 variations. R^2 for COARE and COAMPS® are both 0.96. The relationship between NSSHG and C_0 becomes less linear when ASTD is thermally stable (Figure 18) shown by the increased scatter in the predictions in this region. This result could imply discrepancies between the models and/or

generally more model uncertainty in stable regimes. The linear relationship appears weakly dependent on the ASTD for neutral and unstable regimes, consistent with the prior result of the weaker relationship between C_0 and ASTD. The NSSHG is a dominant factor influencing C_0 and therefore EDS.

The strongest relationship between C_0 and evaluated thermodynamic properties is with NSSHG (Table 1). The viability of the linear relationship between NSSHG and C_0 (Figure 18) relies on how NSSHG is calculated. To explore this concept, two additional separate variations of NSSHG are calculated for COAMPS®: (i) NSSHG based on points at $z = 0.1Z_d$ and $z = 2Z_d$ and (ii) NSSHG based on points at $z = 0.25Z_d$ and $z = 2Z_d$. These will be referred to as $NSSHG_{0.1}$ and $NSSHG_{0.25}$, respectively. Recall, NSSHG in Figure 18 is computed between the surface and $2Z_d$. Note the average EDH for the COAMPS® dataset is 9m.

The relationship between C_0 and $NSSHG_{0.1}$ notably has two distinct behaviors; a portion of $NSSHG_{0.1}$ follow the same trend as NSSHG, and the rest deviates (Figure 19A). Thus, by an altitude of $0.1Z_d$ a reliable relationship between C_0 and NSSGH breaks down indicating the importance of the near surface region. Notably cases with low EDHs (Z_d < ~9 m) follow the same trend as NSSHG (Figure 19B). For these cases, the altitude $0.1Z_d$ is less than 1m above the sea surface, making it remarkably similar to NSSHG. This result suggests that the very near surface region (z <~1m) is critical for the prediction of the duct shape (C_0). Additionally, this result might also suggest that C_0 prediction only requires a measurement within the lowest meter of altitude versus a precise surface measurement. By an altitude of $0.25Z_d$, the variation of specific humidity with height has greatly diminished likely indicating the presence of the constant flux layer.

5.3 Empirical EDS Model

The EDS model utilizes the line of best fit between C_0 and NSSHG, for the COAMPS® data (Figure 20); the COAMPS® data were selected in isolation because it is a denser dataset than COARE and overall, the nonlinear least square regression was able to better replicate this dataset (§4.2.1; Figure 11). This linear fit is:

$$C_0 = -1.241\psi_s - 0.00131 \quad (20)$$

C_0 is predicted via Eqn. 20 and subsequently used in the two-layer refractivity model (Penton and Hackett, 2018; Eqn. 7) to estimate a refractivity profile using a known surface refractivity, EDH, and mixed layer slope; recall, this approach is the EDS model.

The EDS model is used to estimate *M* profiles for 33 *in-situ* ED MAPS polynomial *M* profiles measured during CASPER-East. Figure 21 shows an example comparing refractivity estimated via the EDS model, estimated using the two-layer refractivity model with the Paulus (1990) neutral C_0, and the measured *in-situ* data including a polynomial fit to that data. Notably, the EDS model fits the MAPS data cloud relatively well but produces a longer near surface refractive gradient "tail" compared to the MAPS polynomial *M* profile (Figure 21A). In this example, the neutral profile seems to under-predict the curvature compared to MAPS polynomial *M* profiles, whereas the EDS model predicts curvature remarkably similar to the MAPS profile until ~1 m to the surface where the EDS model predicts much larger surface gradients resulting in a tighter curvature. Residuals between each compared profile are calculated within the "curvature zone" - 0.5m to $2Z_d$ (Figure 21B) - by subtracting the compared profile from the MAPS polynomial M profiles. Residuals are only calculated within the curvature zone to exclude the "tails"; thus, the overall main curvature shape is evaluated instead of being skewed by the known

differences in near surface gradients.

Figure 22 shows the residuals over all 33 MAPS datasets. The neutral C_0 dataset has more positive residuals, indicating a neutral C_0 value under predicts curvature compared to the curvature observed in the MAPS polynomial *M* profiles; the negative EDS model residuals indicate the EDS model generates a tighter curvature than observed in the MAPS polynomial *M* profiles (Figure 22). Overall, *M* profiles calculated using the neutral C_0 and the EDS model have an approximately normal distribution of residuals.

5.4 Simulated Propagation Loss Comparison

As previously discussed in §2.4, limitations of measurement equipment to measure in the lowest few meters above the sea surface require the use of near surface estimation methods such as linear extrapolation, polynomial fits, and MOST to extend data to the sea surface. Notably when comparing near surface estimation methods, the main difference between the data extrapolation methods and those based on MOST or semi-empirical models (i.e., EDS) is the much larger surface gradients in the latter (Figure 23). Wang et al. (2018) and Pastore et al. (2021) discuss limitations of the MAPS polynomial profiles in capturing the expected large surface gradients in this region. MOST and EDS profiles always have larger surface gradients although the shape of the curve in this region can vary between them.

Figure 24 is an example of simulated long range PL for all near surface estimation methods compared to the *in-situ* PL measurements for the MAPS polynomial *M* profile obtained 13 October at 16:49 UTC and the closest *in-situ* radar data obtained on 14 October at 00:57 UTC. The linear and polynomial extrapolation methods are the most similar to each other (Figure 23) and therefore also have the most similar PL predictions (Figure 24; Table 2). RMSEs between simulated and *in-situ* PL are shown in Figure 25. MAPS polynomial *M*

profiles and linear extrapolation of MAPS polynomial *M* profiles from 3m to the surface have the lowest RMSEs for most of the datasets examined, particularly prior to 17 October. Notably, atmospheric conditions are close to a neutral thermal regime until 17 October where the regime then suddenly becomes unstable due to the passage of a cold front on 18 October (Figure 7C).

One interpretation of this trend is that preserving *in-situ* data closer to the surface is critical to accurately predict PL. There were no apparent trends found between RMSE and NSSGH, ASTD, or duration between the time of radar measurements and that of the corresponding MAPS measurements. A future study could investigate these potential trends further with more intricate statistical methods such as principal component analysis.

To evaluate whether the RMSEs between the EDS model and other methods are significantly different in a statistical sense, a two-sample t-test is used. The test requires RMSE populations to each be normally distributed, which was evaluated by comparing the mean and median of each population (Table 2). The mean and median RMSE of each RMSE population varied between ~ 0.4-2.5 dB, which is less than the commonly accepted "baseline error" of ~5 dB for measured RF data (Goldhirsh and Dockery, 1998). Notably, Pastore et al. (2021) considered significant differences in PL to be >20 dB, which is much greater than the differences between the mean and median of the RMSE populations. Given that the mean and median of each population are approximately equal, it is assumed that the data are normally distributed and thus the two-sample t-test is valid to compare RMSE populations.

The critical value for the two-sample t-test between the RMSEs of the EDS model and the other three near surface estimation methods is 2.024; the t-statistics for the linear

extrapolation of the MAPS polynomial *M* profiles and MAPS polynomial *M* profiles are 2.68 and 2.29, respectively, which are greater than the critical value and therefore reject the null hypothesis (i.e., EDS model RMSEs = MOST model RMSEs). The t-statistic of MOST is 0.43 which is less than the critical value; therefore, the null hypothesis is accepted. Thus, the EDS model is not significantly different than MOST but is for the MAPS polynomial *M* profiles and linear extrapolation of the MAPS polynomial *M* profiles (Table 3). Note, when the p-value of a two-sample t-test is larger than the significance level, there is little to no evidence that the means of the two compared populations (i.e., EDS and compared method of near surface refractivity estimation) are statistically different.

The lower RMSEs of the extrapolation-based techniques relative to that of the EDS and MOST models indicates that the extrapolation-based techniques result in PL predictions that more closely match the *in-situ* radar measurements (Table 2). These results reject this study's third research hypothesis (§3) that EDS profiles produce closer PL predictions to *in-situ* PL than alternative methods – although the EDS model's accuracy was similar to the other methods. Perhaps linear extrapolation and MAPS polynomial methods result in propagation predictions that are more similar to the *in-situ* radar data because these methods utilize *in-situ* data closer to the surface. Since the average RMSEs for EDS and MOST are not statistically different, the EDS model is a convenient alternative to MOST (as it requires fewer supporting measurements) for estimating near surface *M* gradients within the MASL for ED scenarios. These estimated gradients can then be utilized for applications such as propagation modeling.

It is also important to contextualize these results based on the nature of the data. The *in-*

situ PL measurements required ~2hrs to collect the ~50 km data in range (Wang et al., 2018; Pastore et al., 2021; Pastore et al., 2022) and the dynamic environment of the MASL can vary considerably during this time frame. Thus, the measured distribution of PL over range is not "instantaneous" in the same sense as the PL model predictions are. Furthermore, each MAPS dataset is collected over a 20-40 min period at one discrete range that varied from 0-11 hours from when the radar data were collected. These varying characteristics of the data imply that none of the estimation methods can represent the "true environment" that the radar data were collected over. Hence, some discrepancies are expected and may not be completely attributable to EDS model shortcomings.

Also note, all data in this study were sourced from the CASPER-East experiment in Duck, North Carolina in October. Future studies in differing locations and seasons should be compared to this study's results to assess how unique the results are to autumn in Duck, North Carolina.

Table 1. Correlation of each examined thermodynamic property and C_0 for both COAMPS® and COARE.

	COAMPS®		COARE	
Thermodynamic Property	**Correlation Coefficient**	**P-Value**	**Correlation Coefficient**	**P-Value**
ASTD	-0.51	0	-0.64	0
NSSHG	-0.98	0	-0.98	0
Wind Shear	-0.56	0	-0.39	0

Table 2. Mean and median RMSE between the PL based on the near surface estimation method and in-situ measurement.

Method	Mean RMSE (dB)	Median RMSE (dB)
MAPS Polynomial Extrapolation	8.51	7.02
EDS Model	12.52	10.01
MOST Model	11.64	11.20
MAPS Linear Extrapolation	7.90	6.63

Table 3. Results of the two-sample t-test comparing RMSEs of EDS model to the other methods.

Method vs EDS	t-Statistic	Critical Value	Statistically Significantly Different	P-Value
MAPS Polynomial Extrapolation	2.29	2.024	YES	0.03
MOST Model	0.43	2.024	NO	0.67
MAPS Linear Extrapolation	2.68	2.024	YES	0.01

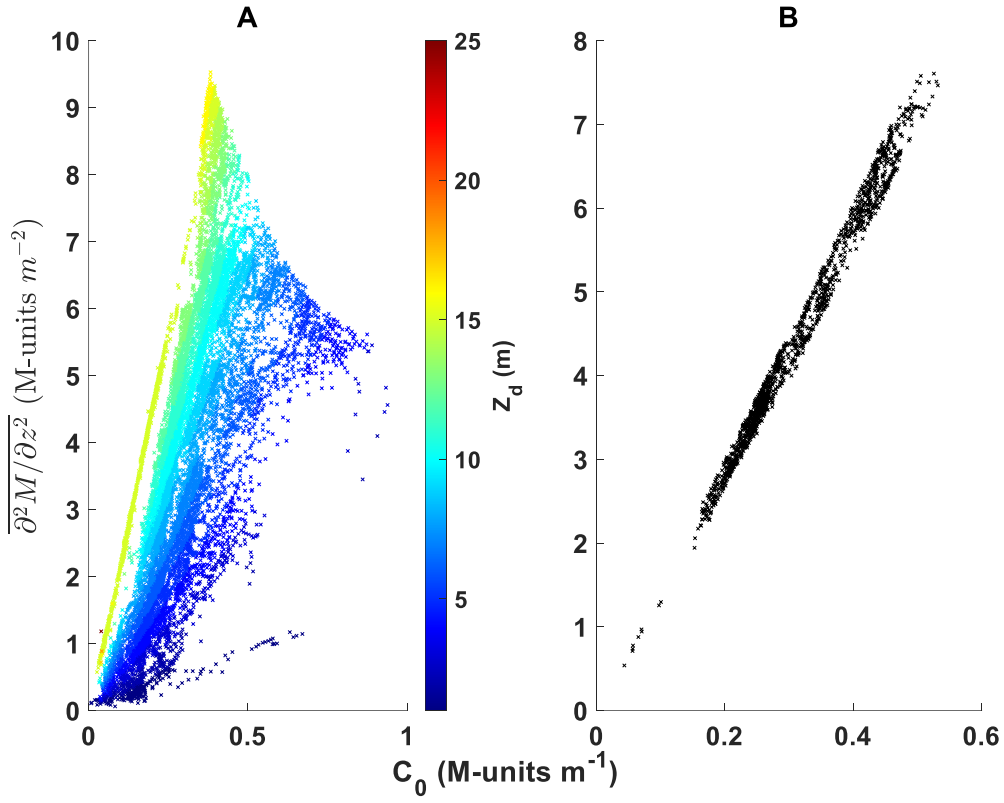

Figure 15. Relationship between the ASOD of each COAMPS® modified refractivity profile with respect to the nonlinear least square's regression fit of C_0. The color of each marker corresponds to the profiles respective duct height. (A) The ASOD is calculated over the entire modified refractivity profile. The linear fit ($\overline{\frac{\partial^2 M}{\partial z^2}} = 11.41C_0 + 0.465$) yields an R^2 value of 0.49 ($R = 0.70$); (B) however fitting the data classified by individual duct heights yields higher R^2 illustrated with black markers showing data for only ~10 m duct heights, yielding an R^2 of 0.99.

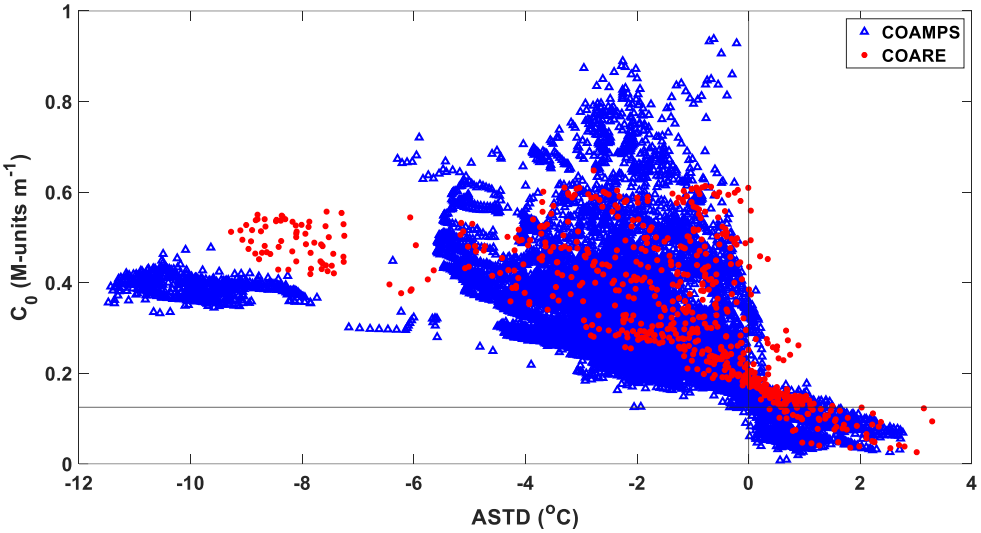

Figure 16. Relationship between ASTD and C_0. The blue triangles represent COAMPS® predictions and the red stars represent COARE predictions. The black vertical line is at neutral ASTD (0 °C) and the black horizonal line is at the neutrally derived Paulus value for C_0 (C_0 = 0.125 M-unit m^{-1}). The R^2 of the COAMPS® data for the line of best fit is 0.26 and the R^2 for COARE is 0.41.

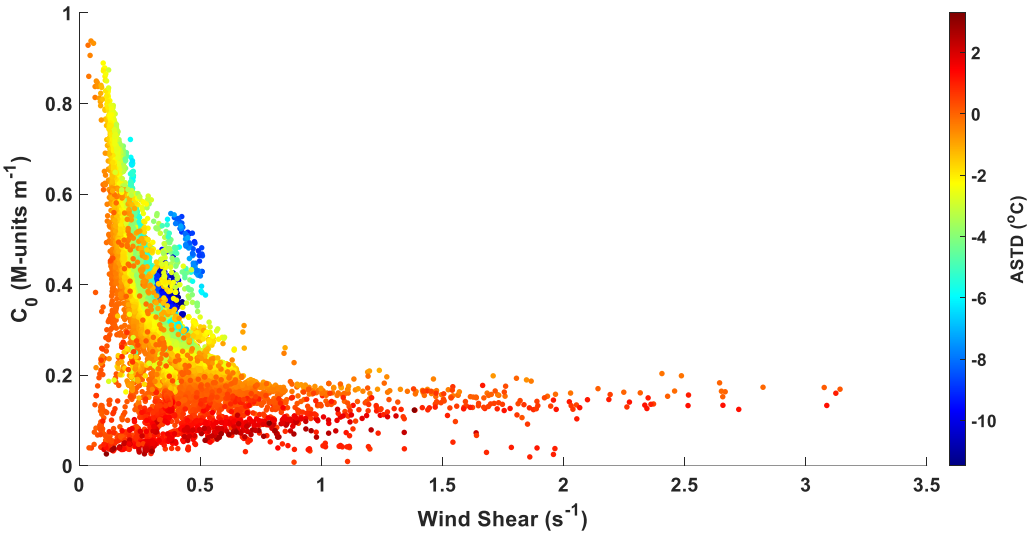

Figure 17. The relationship between C_0 and wind shear for both COARE and COAMPS®. The color of each marker corresponds to the respective ASTD (see colorbar).

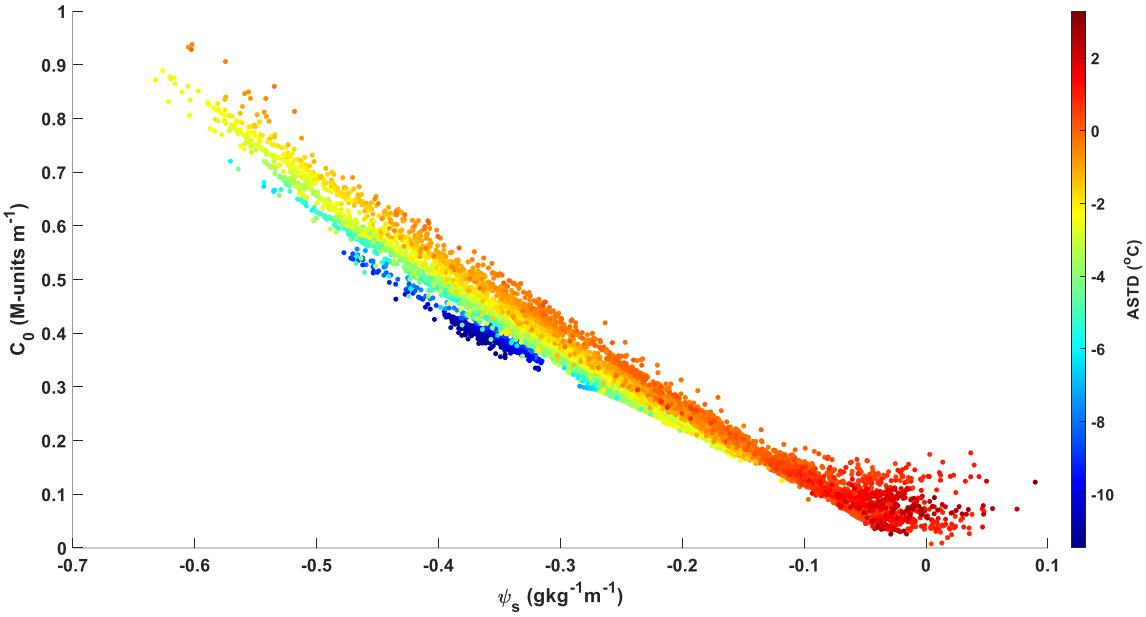

Figure 18. The relationship between the NSSHG and C_0 where the color of each marker is the respective ASTD for both COARE and COAMPS®.

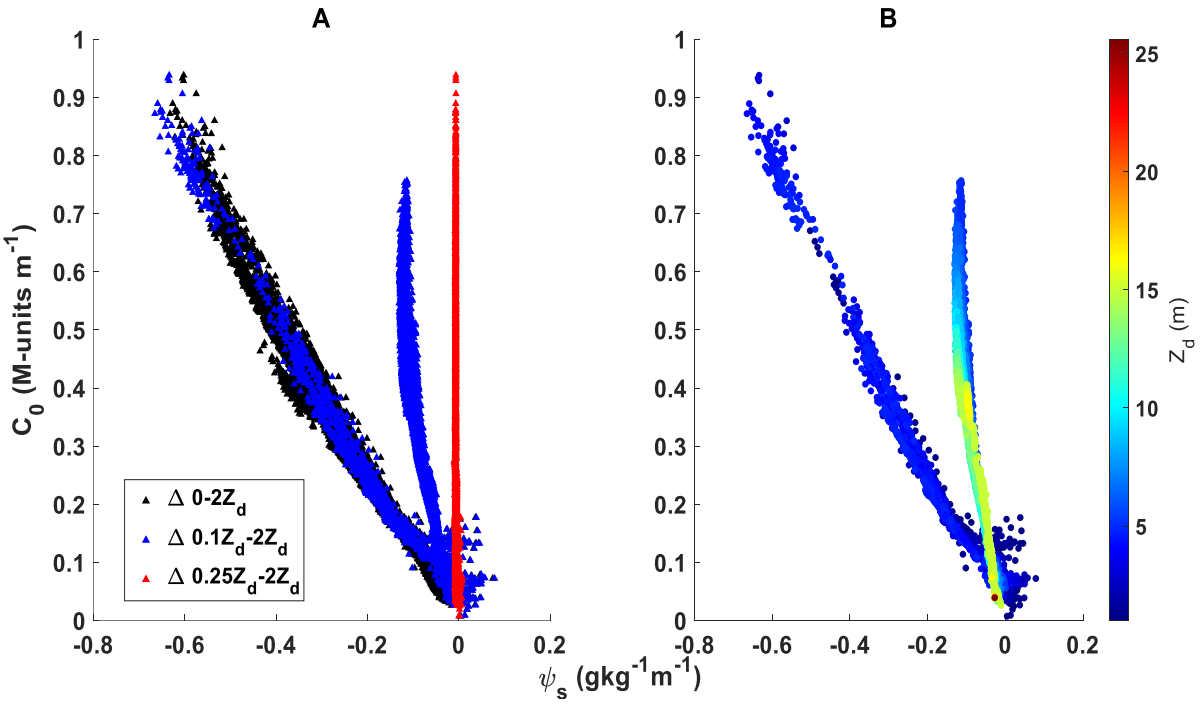

Figure 19. (A) Relationship between C_0 and NSSHG estimated over various altitude ranges for COAMPS® where the colors of the markers represent over which altitudes NSSHG was calculated (see legend). Black markers are between the surface and $2Z_d$, the blue markers are between $1/10^{th}Z_d$ and $2Z_d$, and the red markers are between $1/4^{th}$ Z_d and $2Z_d$. (B) The relationship between the $NSSHG_{1.0}$ and C_0 where the color of each marker is the respective Z_d (see colorbar).

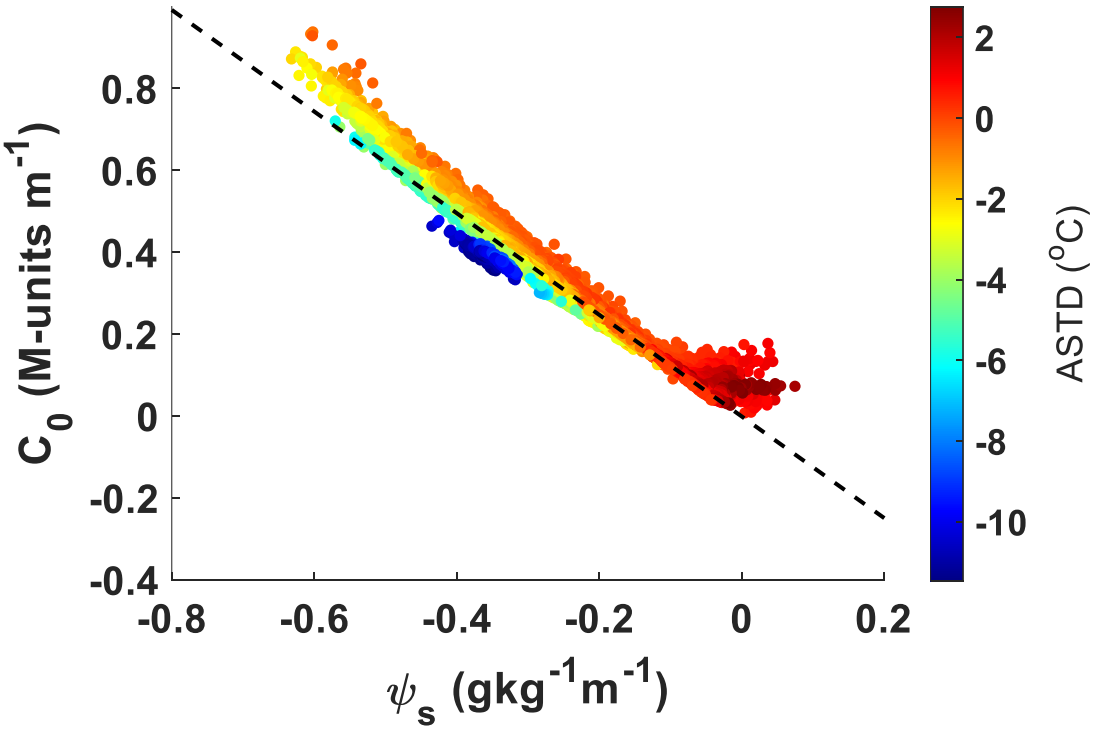

Figure 20. Same as Figure 18 but only COAMPS® with the line of best fit shown between the NSSHG and C_0 with an R^2= 0.96.

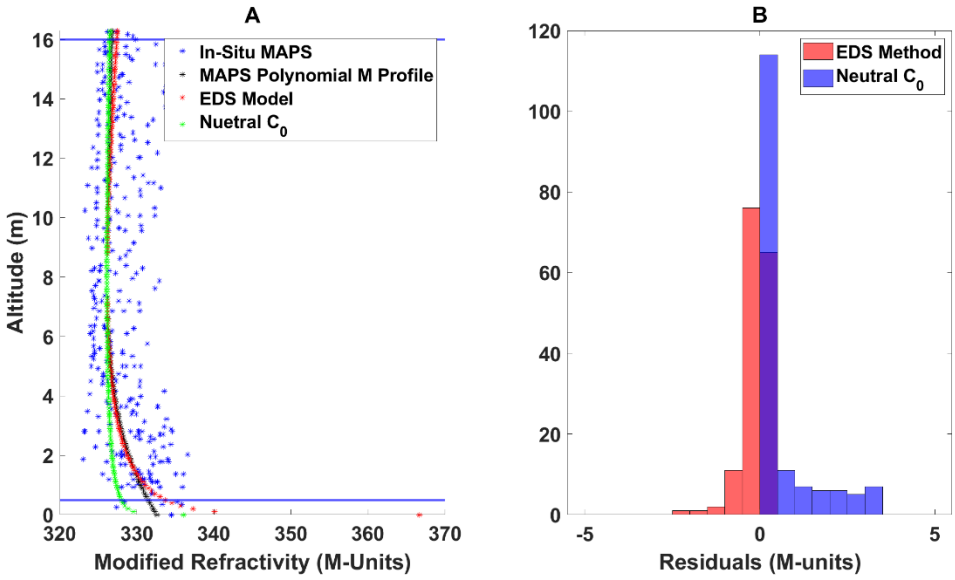

Figure 21. (A) Example modified refractivity profiles from the EDS model (C_0 = 0.512 M-units m^{-1}), the two-layer model using a neutral C_0 (C_0=0.125 M-units m^{-1}), and the 7th order polynomial fit of the in-situ MAPS data from Wang et al., (2018) for 15 October 2015, at 15:03:40 UTC which has an EDH of 8m. (B) A histogram of the residuals between the refractivity based-on the 7th order polynomial fit and the EDS model, and the residuals between the refractivity based on the 7^{th} order polynomial fit and the profile calculated using the neutral C_0 of Paulus (1990) . The residuals are calculated within the "curvature zone" for the data shown in (A), which is bounded by the two horizontal blue lines in (A). The bottom blue line is at an altitude of 0.5m and the top blue line is at $z = 2Z_d$.

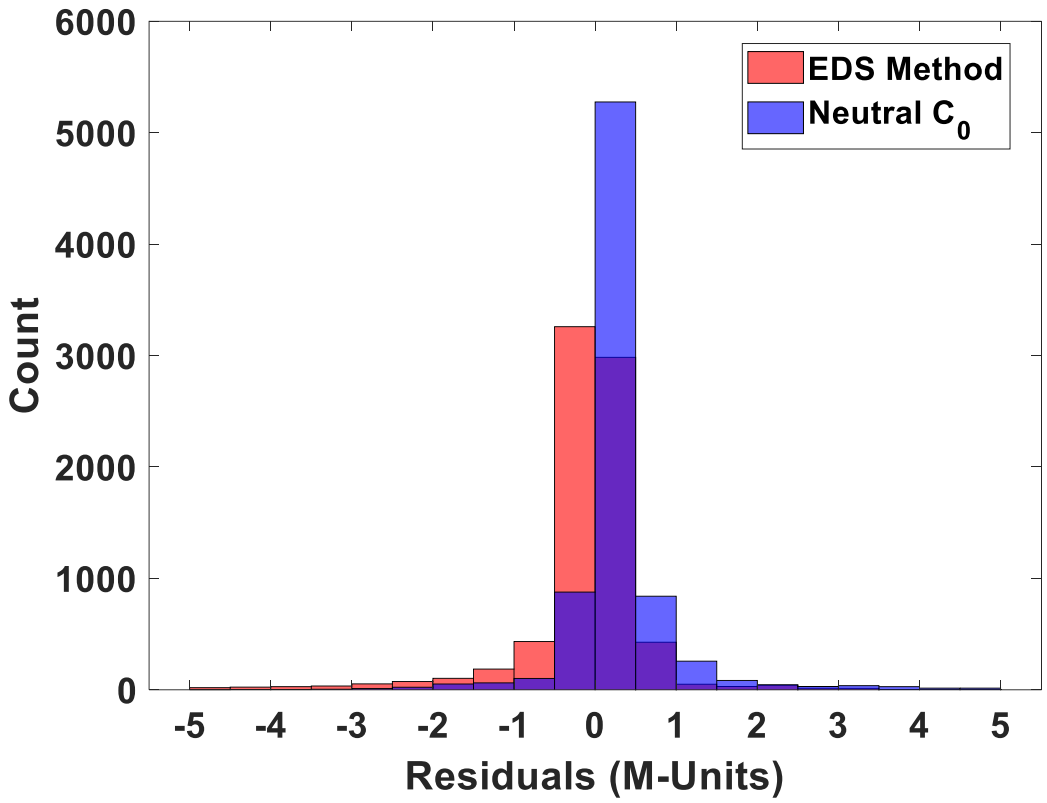

Figure 22. Histograms of refractivity residuals for all data between z =0.5m to $2Z_d$. The residuals are computed between EDS modeled and 7th order polynomial (Wang et al., 2018) modified refractivity profiles in red, and between the two-layer model with neutral curvature and 7th order polynomial (Wang et al., 2018) modified refractivity profiles in blue.

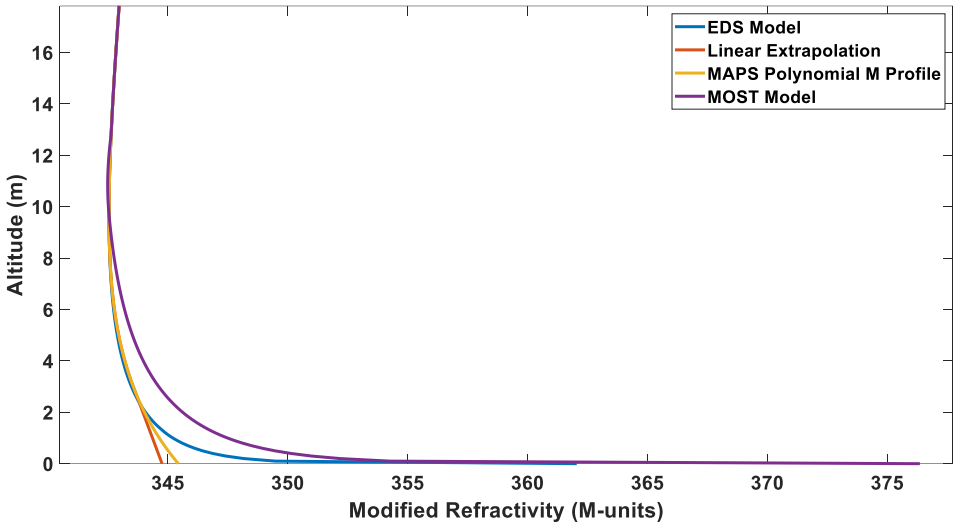

Figure 23. Example modified refractivity profiles that are utilized to simulate PL in VTRPE. The EDS and MOST profiles are blended with the 7th order MAPS polynomial M profiles around an altitude of 9.7m using the weighted average technique (§4.2.3).

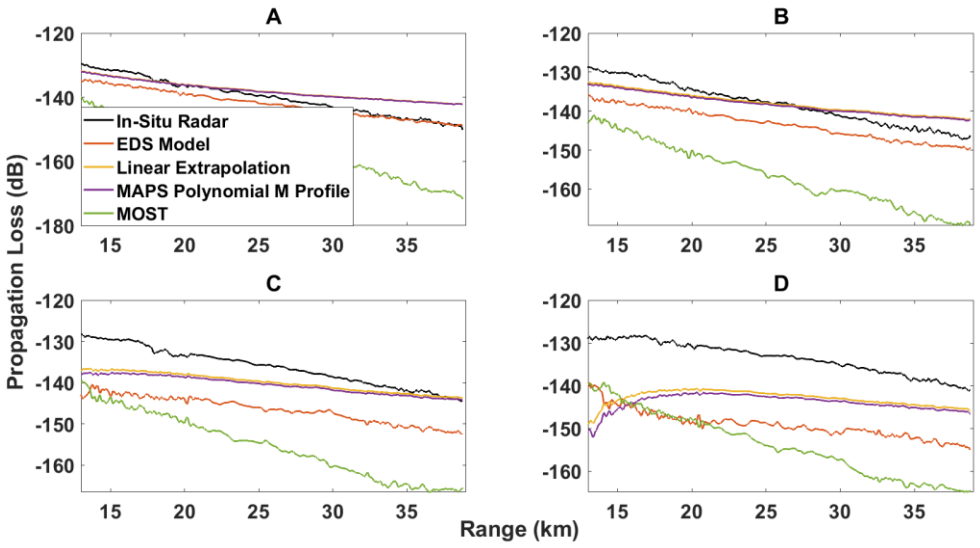

Figure 24. PL of the in-situ measurements and the simulated PL using refractivity based on the various near-surface estimation methods (see legend) versus range for the MAPS profile obtained 13 October at 16:49 UTC and the closest in-situ radar data obtained on 14 October at 00:57 UTC. PL is shown for the four in-situ receiver heights: (A) Rx = 4m, (B) Rx = 6m, (C) Rx = 9m, and (D) Rx = 12m.

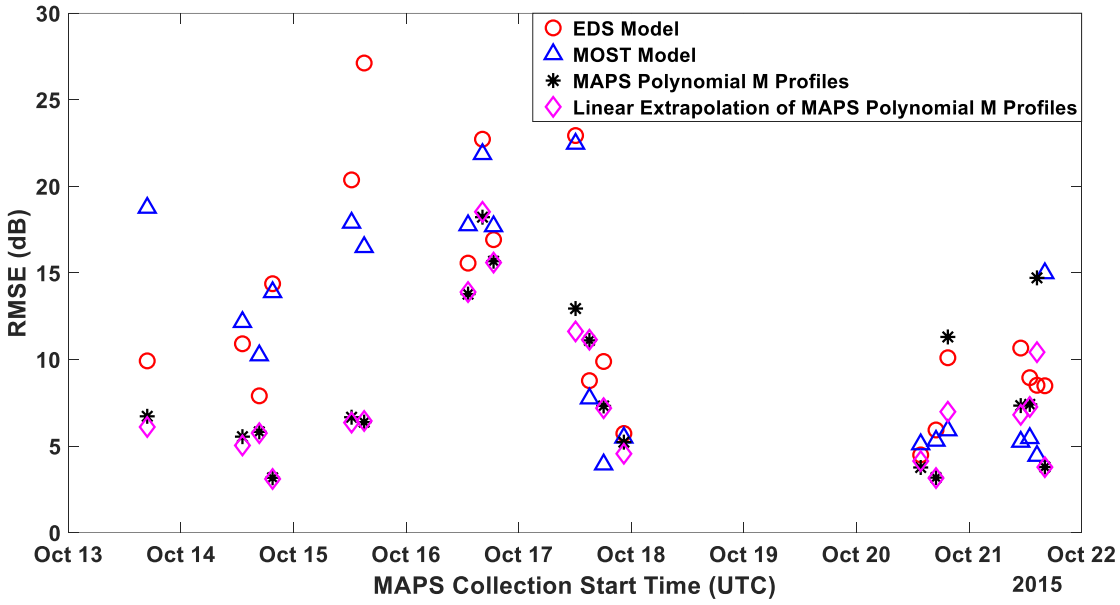

Figure 25. RMSEs between in-situ and simulated PL for all near surface estimation methods (see legend).

6.0 Summary

The MASL is a highly dynamic environment where atmospheric refractivity is varied by changes in pressure, temperature, and humidity. Certain atmospheric conditions create EM trapping layers (i.e., EDs) that can cause anomolous EM propagation. EDs trap EM signals close to Earth's surface, which causes unaccounted-for range increases in radar systems leading to target positioning errors. To account for these anomolies, accurate estimations of EDH and corresponding near surface refractive gradients are essential.

Currently, technologies that meausure near-surface (i.e., within the first few meters of altitude) thermodynamic properties struggle to resolve small vertical variations due to many factors such as waves, sea spray, and platform and sensor housing interference; these limitations lead to data gaps in the near-surface region making the estimation of refractive gradients in this region difficult and thus, modeling techniques for ED estimation are essential. Commonly, logarithmic-linear parametric models are used to describe EDs with altitude (Paulus, 1990; Gersoft et al., 2003; Saeger et al., 2015). This study uses a two-layer logarithmic-linear parametric refractivity model proposed by Penton and Hackett (2018) to describe EDs via three paramters: EDH, ED curvature (C_0), and mixed layer slope.

Prior to this study, the physical significance of C_0 was unknown and reguarly assumed to be a value derived by Paulus (1990) (0.125 M-units m^{-1}) under the assumption of a rarely-oberserved neutral atmosphere (Babin et al.,1997; Rogers et al., 2000; Gerstoft et al., 2003;

Zhang et al., 2011; Wang et al., 2019) limiting their application in different thermal stabilities.

To increase the understanding of C_0 variatons in non-neutral environments, this study determines the physical drivers of C_0, creates a novel model that predicts C_0 via minimal environmental measurements, and uses that model to extend *in-situ* data to the surface with reasonable accuracy for the purposes of propagation predictions. To accomplish these goals, numerical data and bulk environmental measurements from the CASPER-East field campaign are used.

ASTD and wind shear have a weak inverse relationship with C_0 for both COARE and COAMPS® data. In unstable regimes C_0 tends to be larger and in stable regimes C_0 tends to be smaller. This result suggests ASTD has some influence on C_0 variations. When wind shear is small, the range of C_0 is large and in times of greater wind shear, C_0 ranges are relatively small. Wind shear varied the most in near neutral to stable conditions, which C_0 was relatively insensitive to, remaining at small values (~0 – 0.1 M-Units m^{-1}); this result may suggest interactions between mechanical mixing and thermal stability result-in thermodynamic gradients remaining similar. It could also be associated with known shortcomings of MOST in stable conditions (Foken, 2006).

NSSHG and C_0 have the strongest inverse relationship for both COARE and COAMPS®. The relationship between NSSHG and C_0 becomes less linear in a stable atmospheric regime and the linear relationship appears weakly dependent on the ASTD for neutral and unstable regimes, which is consistent with the previously noted weak relationship between C_0 and ASTD. As suggested by the high correlation coefficient, NSSHG is potentially the

primary driver of variations in C_0; thus, a linear function between C_0 and NSSHG is calculated that can predict C_0 from the NSSHG.

Predicted C_0 from the linear function are utilized within the two-layer refractivity model (Penton and Hackett, 2018) to estimate refractivity - this procedure is known as the EDS model. Refractivity based-on a neutral C_0 generates a slightly broader curvature than that observed in the measured MAPS polynomial *M* profiles. The EDS model's predicted C_0 are larger than the neutral value and typically generate a slightly tighter curvature than observed in the MAPS polynomial *M* profiles. Overall, residuals between the MAPS polynomial *M* profiles and the EDS model have an approximately normal distribution with a small residual (~1 M-unit); thus, the EDS model gives reasonable estimation of near surface refractivity.

M profiles estimated via the EDS model and other methods of near surface refractivity estimation (MOST, linear extrapolation, and polynomial extrapolation) are compared in terms of propagation prediction. The EDS model and MOST *M* profiles have the steepest near surface refractivity gradients compared to the linear and polynomial extrapolations. This discrepancy could be due to the extrapolations being strictly mathematical and not incorporating the complexities of the environment that involve steep humidity gradients at the very lowest altitudes.

PL is simulated for all *M* profile estimation methods and compared to *in-situ* PL data via RMSE. The PL RMSEs associated with the EDS model are evaluated against the other near surface estimation methods RMSEs using two-sample t-tests. EDS and MOST PL RMSEs are statistically similar, whereas EDS PL RMSEs differ from that of linear and polynomial extrapolated profiles.

The linear and polynomial extrapolated profiles have smaller mean RMSEs relative to the EDS model. Recall, these mathematical methods utilize *in-situ* data closer to the surface than the MOST or EDS model. This result suggests employing *in-situ* data closer to the surface is always better than using a model for accurately predicting PL. Since the EDS model and MOST are not statistically different, the EDS model is a convenient alternative to MOST when estimating near surface refractivity gradients (within the evaporation layer) for use in propagation modeling, as the EDS model requires fewer supporting measurements relative to MOST.

Future research should be conducted to evaluate the integrity of these results in other regions of the world in various seasons. Furthermore, evaluating the relationship between C_0 and these thermodynamic variables considering heterogenous environments would be advantageous as this study assumed a homogenous environment.

7.0 References

Alappattu, D. P., Wang, Q., Rainer, R., Yamaguchi, R., & Lind, R. J. (2016). Characteristics of surface layer scalar profiles using the in-situ measurements from an undisturbed marine environment. 22nd conference on air-sea interaction. American Meteorological Society. Retrieved from https://ams.confex.com/ams/21SATMET20ASI/webprogram/Paper297336.html

Babin, S. M., & Dockery, G. D. (2002). LKB-based evaporation duct model comparison with buoy data. *J. Appl. Meteorol.*, 41, 434-446.

Babin, S. M., Young, G. S., & Carton, J. A. (1997). A new model of the oceanic evaporation duct. *J. Appl. Meteorol. Climatol*, *36*(3), 193-204.

Banner, M.L., Jones, I.S., & Trinder, J.C. (1989). Wavenumber spectra of short gravity waves. *J. Fluid Mech.,* 198, 321-344.

Bean, B.R., & Dutton, E.J. (1968). *Radio Meteorology*, New York, Dover, 435.

Buck, A.L. (1981). New equations for computing vapor pressure and enhancement factor. *J. Appl. Meteorol.*, 20(12), 1527–1532.

Businger, J.A., Wyngaard, J.C., Izumi, Y., & Bradley, E.F. (1971). Flux profile relationships in the atmospheric surface layer. *J. Atmos. Sci.*, 28, 181–189.

Ding, J., Fei, J., Huang, X., Cheng, X., He, H., Yuan, B., & Liang, Z. (2020). Validation of Evaporation Duct Model in Coastal Regions with ASIT Data. *Journal of Coastal Research*, *99*(SI), 270-281.

Donelan, M.A., Hamilton, J., & Hui, W.H. (1985). Directional spectra of wind generated waves. *Philos. Trans. R. Soc., A315*, 509– 562.

Elliott, W. P., & Gaffen, D. J. (1991). On the utility of radiosonde humidity archives for climate studies. *Bull. Amer. Meteor. Soc.*, 72(10), 1507-1520.

Fairall, C.W., Bradley, E.F., Rogers, D.P., Edson, J.B., & Young, G.S. (1996). Bulk parameterization of air-sea fluxes for tropical ocean-global atmosphere coupled-ocean 91 atmosphere response experiment. *J. Geophys. Res. Oceans*, 101(C2), 3747-3764.

Fairall, C.W., Bradley, E.F., Hare, J.E., Grachev, A.A., & Edson, J.B. (2003). Bulk parameterization of air-sea fluxes: updates and verification for the COARE algorithm. *J. Clim.*, 16 (4), 571-591.

Foken, T. (2006). 50 Years of the Monin–Obukhov Similarity Theory. *Boundary-Layer Meteorol.*, 119**,** 431–447 https://doi.org/10.1007/s10546-006-9048-6

Freehafer, J.E., Fishback, W.T., Furry, W.H., & Kerr, D.E. (1951). Propagation of Short Radio Waves. McGraw-Hill, London, 728.

Frederickson, P. A. (2015). Software Design Description for the Navy Atmospheric Vertical Surface Layer Model (NAVSLaM), Version 1.1. Prepared for the Naval Oceanographic Office. *Systems Integration Division.*

Frederickson, P. (2016). Navy atmospheric measurements for EM propagation modeling. (Executive summary). Naval Postgraduate School

Friis, H.T. (1946). A note on a simple transmission formula. *Proc. IRE*, 34, 254-256 pp.

Garratt, J. (1992). The Atmospheric Boundary Layer. *Cambridge University Press.*

Gerstoft, P., Rogers, L.T., Krolik, J.L., & Hodgkiss, W.S. (2003). Inversion for refractivity

parameters from radar sea clutter. *Radio Sci.*, 38(3).

Goldhirsh, J., & Dockery, G.D. (1998). Propagation factor errors due to the assumption of lateral homogeneity. *Radio Sci.*, 33(2), 239– 249.

Haack, T., Wang, C., Garrett, S., Glazer, A., Mailhot, J., & Marshall, R. (2010). Mesoscale modeling of boundary layer refractivity and atmospheric ducting. Journal of Applied Meteorology and Climatology, 49(12), 2437–2457. https://doi.org/10.1175/2010jamc2415.1

Halliwell, G.R. (2004). Evaluation of vertical coordinate and vertical mixing algorithms in the HYbrid Coordinate Ocean Model (HYCOM). *Ocean Model.*, 7(3-4), 285-322

Hodur, R.M. (1997). The Naval Research Laboratory's Coupled Ocean/Atmosphere Mesoscale Prediction System (COAMPS®). *Mon. Weather Rev.*, 125, 1414-1430.

Hogan, T. F., Liu, M., Ridout, J. A., Peng, M. S., Whitcomb, T. R., Ruston, B. C., Reynolds, C. A., Eckermann, S. D., Moskaitis, J.R., Baker, N.L. and McCormack, J.P. (2014). The navy global environmental model. Oceanography, 27(3), 116–125. https://doi.org/10.5670/oceanog.2014.73

Ortiz-Suslow, D. G., & Wang, Q. (2019). An evaluation of Kolmogorov's −5/3 power law observed within the turbulent airflow above the ocean. *Geophys. Res. Lett.*, 46 https://doi.org/10.1029/ 2019GL085083

Karimian, A., Yardim, C., Haack, T., Gerstoft, P., Hodgkiss, W. S., & Rogers, T. (2013). Toward the assimilation of the atmospheric surface layer using numerical weather prediction and radar clutter observations. *J. Appl. Meteorol. Clim.*, 52(10), 2345-2355.

Kang D, & Wang Q. (2016). Optimized estimation of surface layer characteristics from

profiling measurements. *Atmosphere*, 7(2), 14.

Kukushkin, A. (2004). Radio wave propagation in the marine boundary layer. Wiley-VCH Verlag GmbH & Co. KGaA, Weinheim, HR, 193.

Lentini, N.E., & Hackett, E.E. (2015). Global sensitivity of parabolic equation radar wave propagation simulation to sea state and atmospheric refractivity structure. *Radio Sci.*, 50(10), 1027-1049.

Matsko, I.J., & Hackett, E.E. (2019). Impact of radar data sampling on the accuracy of atmospheric refractivity inversions over marine surface. *Radio Sci.*, 54(7), 704-714.

McKeon, B. D. (2013). Climate analysis of evaporation ducts in the south China sea. (M.S. Thesis). Naval Postgraduate School, Monterey, United States.

Monin, A. S., & Obukhov, A. M. (1954). Basic laws of turbulent mixing in the surface layer of the atmosphere. *Contrib. Geophys. Inst. Acad. Sci. USSR*, 151(163), e187.

Pastore, D. M., Greenway, D. P., Stanek, M. J., Wessinger, S. E., Haack, T., Wang, Q., & Hackett, E. E. (2021). Comparison of atmospheric refractivity estimation methods and their influence on radar propagation predictions. Radio Science, 56(9), 1–17. https://doi.org/10.1029/2020rs007244

Pastore, D. M., Wessinger, S. E., Greenway, D. P., Stanek, M. J., Burkholder, R. J., Haack, T., Wang, Q., Hackett, E. E. (2022). Refractivity inversions from point-to-point X-band radar propagation measurements. *Radio Sci.*, 57, e2021RS007345. https://doi.org/10.1029/2021RS007345

Paulus, R.A. (1990). Evaporation duct effects on sea clutter. *IEEE Trans. Antenn. Propag.*, 38(11), 1765-1771.

Paulus, R.A. (1991). Validation of the bulk method for overwater optical refractivity.

NOSC Technical Report 1462.

Peixoto, J.P., & Oort, A.H. (1996). The climatology of relative humidity in the atmosphere. *J. Clim.*, 9, 3443–3463.

Penton, S.E., & Hackett. E.E. (2018). Rough ocean surface effects on evaporative duct atmospheric refractivity inversions using genetic algorithms. *Radio Sci*., 53(6), 804-819.

Pierson Jr, W.J., & Moskowitz, L. (1964). A proposed spectral form for fully developed wind seas based on the similarity theory of SA Kitaigorodsky. *J. Geophys. Res.*, 69(24), 5181-5190.

Rainer, R. B. (2016). In-situ observation of undisturbed surface layer scaler profiles for characterizing evaporative duct properties (M.S. Thesis). Naval Postgraduate School, Monterey, United States.

Rogers, L., Hattan, C., & Stapleton, J. (2000). Estimating evaporation duct heights from radar sea echo. *Radio Sci.*, 35(4), 955–966.

Ross, R.J., & Elliot, W.P. (1996). Tropospheric water vapor climatology and trends over North America: 1973-93. *J. Clim.*, 9, 3561-3574.

Ryan, F. J. (1991). Analysis of electromagnetic propagation over variable terrain using the parabolic wave equation (No. NOSC/TR-1453). Naval Ocean Systems Center, San Diego, CA.

Saeger, J.T., Grimes, N.G., Rickard, H.E., & Hackett, E.E. (2015). Evaluation of simplified evaporation duct refractivity models for inversion problems. *Radio Sci.*, 50(10), 1110-1130.

Sirkova, I. (2012). Brief review on PE method application to propagation channel modeling

in sea environment. *Open Eng.*, 2(1), 19-38.

Skolnik, M.I. (1990). Radar Handbook, McGraw-Hill, New York, NY.

Skolnik, M.I. (2003). Introduction to Radar Systems, 3rd ed., McGraw-Hill New York, NY.

Thews, E.R. (1990). Timely prediction of low-altitude radar performance in operational environments using in situ atmospheric refractivity data. In IEE Proceedings F (Radar and Signal Processing), 137(2), 89-94.

Trahan, J.W. (1995). IR Refraction and Mirages. Presented at 1995 IRIS-TBD Conference, 1, 185.

Wang, Q., Alappattu D.P., Billingsley S., Blomquist B., Burkholder R.J., Christman A.J., Creegan E.D., de Paolo T., Eleuterio D.P., Fernando H.J., Franklin K.B., Grachev A.A., Haack T., Hanley T.R., Hocut C.M., Holt T.R., Horgan K., Jonsson H.H., Hale R.A., Kalogiros J.A., Khelif D., Leo L.S., Lind R.J., Lozovatsky I., Planella-Morato J., Mukherjee S., Nuss W.A., Pozderac J., Ted Rogers L., Savelyev I., Savidge D.K., Kipp Shearman R., Shen L., Terrill E., Marcela Ulate A., Wang Q., Travis Wendt R., Wiss R., Woods R.K., Xu L., Yamaguchi R.T., & Yardim C. (2018). CASPER: coupled air–sea processes and electromagnetic ducting research. *Bull. Amer. Meteor. Soc.*, 99, 1449–1471.

Wang, Q., Burkholder, R.J., Yardim, C., Xu, L., Pozderac, J., Christman, A., Fernando, H.J., Alappattu, D.P., & Wang, Q. (2019). Range and Height Measurement of X-Band EM Propagation in the Marine Atmospheric Boundary Layer. *IEEE Trans. Antennas Propag.*, 67, 2063-2073.

Zhang, J.-P., Wu, X.-S., Zhu, Q.-L., & Wang, B. (2011). A four-parameter M profile model

for the evaporation duct estimation from radar clutter. *Prog. Electromagn. Res.*, 114, 353–368.

Appendix

The non-dimensional universal functions of MOST (Monin and Obukhov, 1954; Garratt, 1992; Foken, 2006) for wind, temperature, and humidity are respectively:

$$\left(\frac{kz}{U_*}\right)\frac{\partial \bar{U}}{\partial z} = \Phi_U\left(\frac{z}{L}\right) \tag{21}$$

$$\left(\frac{kz}{T_*}\right)\frac{\partial \bar{T}}{\partial z} = \Phi_T\left(\frac{z}{L}\right) \tag{22}$$

$$\left(\frac{kz}{q_*}\right)\frac{\partial \bar{q}}{\partial z} = \Phi_q\left(\frac{z}{L}\right) \tag{23}$$

where Φ are universal stability functions for wind, temperature, and humidity denoted via subscripts of *U*, *T*, and *q*, respectively. Note that it is typically assumed that $\Phi_T = \Phi_q$.